AIAA/AAS Astrodynamics Specialist Conference
2 - 5 August 2010, Toronto, Ontario Canada

AIAA 2010-7524

Optimal Impulsive Escape Trajectories from a Circular Orbit to a Hyperbolic Excess Velocity Vector

D.R. Jones* and C. Ocampo†

The University of Texas at Austin, Austin, TX, 78712

Feasible impulsive transfers from a circular parking orbit to some hyperbolic excess velocity vector are constructed, and used as initial guesses in solving corresponding, minimum ΔV, constrained parameter optimization problems. Much attention is devoted to quantifying and enhancing the proximity of the feasible escape to the optimal, thereby improving convergence. The impulsive solutions may be further utilized as initial guesses for a procedure to determine optimal, finite-burn, continuous transfers between celestial bodies. Significant fuel costs associated with certain escape geometries motivates in-depth understanding of this fundamental optimization problem. Reducing these costs provides increased: landing site coverage, abort capability, and parking orbit geometries which may have otherwise not met mission constraints. 1-impulse and 3-impulse (time-of-flight free and fixed) escapes are presented, which exhibit improved feasible to optimal proximity when compared with past methods. Furthermore, qualitative criteria are developed, which indicate the number of impulses to use (1, 3, or the potential addition of a 4th), as functions of the escape geometry. Although emphasis is placed on Moon-to-Earth returns, all parameters are made non-dimensional such that the results and qualitative criteria presented are applicable to generalized departures from a circular orbit about any celestial body.

Nomenclature

$_i$ and $_j$	subscripts indicating orbit (0 to f) or maneuver number (1 to N)
e_i and a_i	eccentricity and semi-major axis of orbit i
$\mathbf{v}_\infty^+$	target outgoing hyperbolic excess velocity vector, with magnitude v_∞^+
TOF	time-of-flight for escape (t_1 to t_f)
t_0 and t_f	initial epoch and time of final maneuver
t_i	time at which maneuver i occurs
J	scalar performance index (total cost), $J = \Delta V = \sum_{i=1}^{N} \Delta v_i$
$\mathbf{X_p}$	parameter vector
$\mathbf{C}$ and $\mathbf{D}$	equality and inequality constraint vectors, respectively
$\Delta\mathbf{v}_i$	impulsive maneuver vector i, with magnitude Δv_i
δ_{rel} and α_{rel}	relative declination and right ascension angles of $\mathbf{v}_\infty^+$ w.r.t. Orbit 0 frame
$\mathbf{r}_{p_i}$ and $\mathbf{r}_{a_i}$	pericenter and apocenter radius vectors of orbit i, with magnitudes r_{p_i} and r_{a_i}
$\mathbf{v}_{p_i}$	pericenter velocity vector of orbit i, with magnitude v_{p_i}
r_{min}	minimum allowable pericenter radius
r_{max}	maximum allowable apocenter radius
$\mathbf{h}_i$	angular momentum vector of orbit i, with magnitude h_i
$\hat{\mathbf{h}}_f^*$	initial selection for the departure hyperbola angular momentum direction, $\hat{\mathbf{h}}_f$
μ	standard gravitational parameter of the central body
ν_∞^+	true anomaly associated with $\mathbf{v}_\infty^+$ on the departure hyperbola
$\mathbf{v}_\infty^-$	incoming hyperbolic excess velocity vector with magnitude v_∞^-

*Graduate Student, Department of Aerospace Engineering and Engineering Mechanics, The University of Texas at Austin, W. R. Woolrich Laboratories 1 University Station, C0600, 210 East 24th Street, Austin, Texas 78712; Student Member, AIAA.

†Associate Professor, Department of Aerospace Engineering and Engineering Mechanics, The University of Texas at Austin, W. R. Woolrich Laboratories 1 University Station, C0600, 210 East 24th Street, Austin, Texas 78712; Member, AIAA.

δ	turning angle of the departure hyperbola
$\mathbf{r}_{\Delta v_i}$	position vector where maneuver i occurs, with magnitude $r_{\Delta v_i}$
ν_{ij}	true anomaly where maneuver i occurs on orbit j
T_{p_i}	time period of orbit i
$\mathbf{v}_\infty^*$	Keplerian propagated outgoing hyperbolic excess velocity vector
X_p^{err}	non-dimensional parameter vector error
θ	minimum angle possible between $\hat{\mathbf{h}}_0$ and $\hat{\mathbf{h}}_f$
ζ	an angle factor which rotates $\hat{\mathbf{h}}_f^*$ to $\hat{\mathbf{h}}_f$ about $\mathbf{v}_\infty^+$
IG	initial guess
$(\hat{})$	normalized vector

I. Introduction

THE problem of transferring from a circular parking orbit to some departure hyperbola $\mathbf{v}_\infty^+$ vector, with minimum ΔV, is a fundamental one in space exploration. Gerbracht and Penzo,[1] who established much of the early work on this topic, consider it to be 'the most important and promising trajectory optimization problem.' Its application provides increased landing site coverage and launch/injection opportunities at celestial bodies, as well as allowing for parking orbits which may have otherwise not met mission constraints due to the large departure/arrival maneuvers they require. This paper is a continuation and improvement upon work presented by Ocampo and Saudemont,[2] and focuses on the robust construction of feasible 1 and 3-impulse escapes which, when used as initial guesses (IG), reliably converge to the minimum ΔV solutions. Poor quality IG escapes, exhibiting different behavior than the optimal, tend to produce convergence problems, a reality which has in part motivated this work. In addition to improving the heritage IG methods in,[2] a new method for targeting a time-fixed 3-impulse escape is presented along with some qualitative analysis indicating the number of impulses to use for particular escape geometries.

Similar to what was done in,[1] parameter optimization (direct method) is used to determine optimal impulsive escapes as opposed to Lawden's primer vector theory (indirect method),[3] which is the impulsive equivalent of the calculus of variations, applicable when the escape time (TOF) is known. In addition to the work of,[1] Gobetz and Doll[4] provide a summary of optimal impulsive transfers and Edelbaum[5] has considered primer optimal 3 and 4-impulse escapes from a circular orbit when the TOF is known.

The problem is easily manipulated to include impulsive captures, where $\mathbf{v}_\infty^+$ is then the incoming excess velocity vector, with the same optimal solution as the escape, but in reverse. For simplicity, attention is restricted to escapes, where a $\mathbf{v}_\infty^+$ vector may correspond to a back-propagated Earth re-entry state or some other post-escape target. Therefore, the optimal impulsive escapes may be propagated and differentially corrected to match continuity with a trajectory from some backward propagated state, and finally converted to an optimal finite burn trajectory as described in.[2] However, the central focus in this work is the development of IG methods which produce escapes in close proximity to their corresponding optimal escapes for a variety of $\mathbf{v}_\infty^+$ vectors, including those involving unfavorably large plane changes.

This paper is organized as follows:

- Section II describes the problem in terms of background and motivation, the assumptions being made, and the type of optimization being performed.
- Section III begins the construction of the 1-impulse and 3-impulse time-free and time-fixed IG escapes and their respective parameter optimization problems. This section begins with derivations applicable to all methods, followed by subsections devoted to each escape: section III-A is devoted to the 1-impulse, followed by the 3-impulse time-free in section III-B, and the 3-impulse time-fixed in section III-C. Each subsection is split into parts: first the construction of the IG followed immediately by the optimization problem. For example, section III-B-1 outlines the 3-impulse time-free IG, followed by the optimization problem in section III-B-2, and an alternate optimization problem in section III-B-3.
- Section IV contains results corresponding to each of the three impulsive escapes methods (e.g. section IV-A contains 1-impulse results, whereas section IV-C contains results applicable to the 3-impulse time-fixed escape). Finally, section IV-D examines the question of how many impulses to use for par-

ticular escape geometries and makes comparisons between the various escape methods (i.e. the number of impulses and time-free vs. time-fixed).

II. Description of the Problem

The problem is described in general terms as follows: given an initial state on a known circular orbit ($e_0 = 0$) about the central body, at some epoch (t_0), determine the optimal impulsive transfer sequence that will take the spacecraft to the specified $\mathbf{v}_\infty^+$ vector. The optimal impulsive escape (of N number of impulses) can be converged upon using a Sequential Quadratic Programming (SQP) algorithm, where a parameter vector $\mathbf{X_p}$ is found which minimizes the total cost (performance index $J = \sum_{i=1}^{N} \|\Delta \mathbf{v}_i\|$) subject to a vector of equality constraints $\mathbf{C}$ and a vector of inequality constraints $\mathbf{D}$. The optimal escape may be either a 1, 3, or 4-impulse sequence, dependent on the particular problem geometry, and some switching criteria.

Two-body orbital dynamics are used throughout in determining the IG solutions and the optimal, thereby avoiding the need for numerical integration of the equations of motion. It is assumed that the presence of 3rd body and/or non-spherical perturbations will only alter the optimal solutions slightly. Escapes from circular parking orbits (a special case of the general ellipse) are given primary attention in this work, but these results may be used in continuation for the more general problem of escape from an ellipse. The 2-impulse escape is omitted in this work, since past work[4] has shown that from a circular parking orbit to any $\mathbf{v}_\infty^+$ vector, the 2-impulse is never simultaneously of lower cost than both the 1 and 3-impulse solutions.

Escapes from the Moon are used as primary numerical examples; however, the methods are general and may be applied to any celestial body. For trans-Earth injection maneuvers from the Moon, Condon et al.[6] has determined a reasonable range of escape asymptotes which vary with v_∞^+ magnitude between 0.8 to 1.3 km/s and relative declinations δ_{rel} from -90° to 90°. These ranges are utilized for much of the numerical results, but to maintain generality and applicability to all escapes from any celestial body the input parameters are made non-dimensional with respect to the pericenter radius r_{p_0} and speed v_{p_0} of the parking orbit. For 3-impulse escapes, in the absence of 3rd bodies, the optimal occurs when the intermediate orbit(s) pericenter and apocenter radii approach zero and infinity, respectively.[4] Therefore, these radii must be constrained during the optimization process, based on problem specific limits: r_{min} and r_{max}. A characteristic escape velocity is then defined as v_∞^+/v_{p_0}, and characteristic radii limits are defined as r_{min}/r_{p_0} and r_{max}/r_{p_0}. Also, throughout this work it is assumed that $r_{min} \leq r_{p_0}$ and $r_{max} > r_{p_0}$. The limits used in the majority of the numerical results were derived to yield a minimum altitude at the Moon of 100-km, and a maximum 1-2 day 3-impulse TOF ($r_{min} > 1838$ km and 17633 km $\leq r_{max} \leq 30000$ km).

Furthermore, a new 3-impulse IG method is developed when the sequence time-of-flight (TOF) is specified. The motivation for this is to provide quick assessments, and potential optimization, of the abort cost as a function of TOF, for a particular $\mathbf{v}_\infty^+$ and parking orbit. The range of TOF used may be proportional to the range of r_{max} used in the time-free problem.

III. General Methodology

The parking orbit perifocal unit vectors ($\hat{\mathbf{r}}_{p_0}$, $\hat{\mathbf{v}}_{p_0}$, and $\hat{\mathbf{h}}_0$) are used to define a body centered and fixed reference frame which serves as the basis for $\mathbf{v}_\infty^+$. Where $\mathbf{h}_0$ is the angular momentum vector of the parking orbit, and $\mathbf{r}_{p_0}$ and $\mathbf{v}_{p_0}$ are the pericenter position and velocity vectors of the parking orbit (all assumed known). $\mathbf{v}_\infty^+$ is then described using spherical angles relative to this frame: declination (δ_{rel}) and right ascension (α_{rel}). And $\mathbf{v}_\infty^+$ is normalized, with respect to its magnitude $\|\mathbf{v}_\infty^+\| = v_\infty^+$.

$$\mathbf{v}_\infty^+ = \|\mathbf{v}_\infty^+\| \begin{pmatrix} \cos\delta_{rel} \ \cos\alpha_{rel} \\ \cos\delta_{rel} \ \sin\alpha_{rel} \\ \sin\delta_{rel} \end{pmatrix} \qquad \hat{\mathbf{v}}_\infty^+ = \frac{\mathbf{v}_\infty^+}{\|\mathbf{v}_\infty^+\|} \tag{1}$$

Also, $v_\infty^+ > 0$ is required so that parabolic escape orbits are excluded. Limiting the parking orbit to be circular further simplifies the problem, making the escapes independent of α_{rel} and the orientation of the parking orbit in inertial space.

For labeling purposes, the initial parking orbit will be called Orbit 0 and Orbit f will be the hyperbolic orbit resulting after the completion of the final maneuver and containing the target $\mathbf{v}_\infty^+$. The number

of intermediate orbits is dependent on the number of impulses: for the 1-impulse escape, there are no intermediary orbits, for the 3-impulse escape there are two intermediary orbits (Orbits 1 and 2). Various orbit parameters will have subscripts $(_0, _1, _2, _3, _f)$ corresponding to these orbits. For the 3-impulse time-free IG, Orbits 0 and 1 will be coplanar with angular momentum direction given by $\hat{\mathbf{h}}_0$, and Orbits 2 and f will be coplanar and normal to $\hat{\mathbf{h}}_f$. Similarly for the 3-impulse time-fixed IG, Orbits 0 and 1 will be coplanar, but Orbit 2 will have angular momentum direction given by $\hat{\mathbf{h}}_2$, which will not necessarily be along $\hat{\mathbf{h}}_f$.

A key component in generating near-optimal IG solutions involves proper selection of $\hat{\mathbf{h}}_f$, which is only required to be normal to $\hat{\mathbf{v}}_\infty^+$. An initial selection of $\hat{\mathbf{h}}_f$, called $\hat{\mathbf{h}}_f^*$ can be made on the basis of three important sub-cases, as is done in much of the literature on this subject including the heritage work of.[2] However, depending on the number of impulses used, as well as the particular escape geometry, $\hat{\mathbf{h}}_f^*$, may be quite far from optimal. The rotation of $\hat{\mathbf{h}}_f^*$ to $\hat{\mathbf{h}}_f$, by an angle ζ about $\hat{\mathbf{v}}_\infty^+$, is an important aspect of the IG improvement developed in this paper. The sub-cases are then:

1. $\left|\hat{\mathbf{h}}_0 \cdot \hat{\mathbf{v}}_\infty^+\right| = 0$ This means that $\hat{\mathbf{h}}_0$ is normal to $\hat{\mathbf{v}}_\infty^+$: no plane change is required. The departure orbit plane can be coincident with the parking orbit plane, and is chosen to be so. In this case, their respective angular momentum vectors are thus collinear, yielding two possible choices: $\hat{\mathbf{h}}_f^* = \pm\hat{\mathbf{h}}_0$.

$$\hat{\mathbf{h}}_f^* = +\hat{\mathbf{h}}_0 \tag{2}$$

   is chosen for a zero angle plane change. The other choice requires a 180° plane change which implies an expensive retrograde maneuver and is thus discarded.

2. $\left|\hat{\mathbf{h}}_0 \cdot \hat{\mathbf{v}}_\infty^+\right| = 1$ This means that $\hat{\mathbf{h}}_0$ is collinear to $\hat{\mathbf{v}}_\infty^+$; they are either in the same or opposite direction: a 90° plane change is required. The departure orbit plane is normal to the parking orbit plane. Any vector normal to $\hat{\mathbf{v}}_\infty^+$ can serve as $\hat{\mathbf{h}}_f^*$, which is also normal to $\hat{\mathbf{h}}_0$. $\hat{\mathbf{h}}_f^*$ is chosen to be

$$\hat{\mathbf{h}}_f^* = \frac{\hat{\mathbf{r}}_{p_0} \times \hat{\mathbf{v}}_\infty^+}{\left\|\hat{\mathbf{r}}_{p_0} \times \hat{\mathbf{v}}_\infty^+\right\|} \tag{3}$$

3. $0 < \left|\hat{\mathbf{h}}_0 \cdot \hat{\mathbf{v}}_\infty^+\right| < 1$ This is the most general case: the departure orbit is neither normal nor coplanar to the parking orbit. $\hat{\mathbf{h}}_f^*$ is chosen to be the unit vector normal to $\hat{\mathbf{v}}_\infty^+$ that is closest to $\hat{\mathbf{h}}_0$, so that the angle between the parking orbit and departure orbit planes is minimized. This is determined from:

$$\hat{\mathbf{h}}_f^* = \frac{\hat{\mathbf{v}}_\infty^+ \times \left(\hat{\mathbf{h}}_0 \times \hat{\mathbf{v}}_\infty^+\right)}{\left\|\hat{\mathbf{v}}_\infty^+ \times \left(\hat{\mathbf{h}}_0 \times \hat{\mathbf{v}}_\infty^+\right)\right\|} \tag{4}$$

   It is noted that, $\hat{\mathbf{h}}_f^*$ is always defined if $0 \leq \left|\hat{\mathbf{h}}_0 \cdot \hat{\mathbf{v}}_\infty^+\right| < 1$ and is along the projection of $\hat{\mathbf{h}}_0$ onto the plane that is normal to $\hat{\mathbf{v}}_\infty^+$, and therefore minimizes the plane change.

Once $\hat{\mathbf{h}}_f$ is determined, the remaining elements of the departure hyperbola can be computed. The semi-major axis is known,

$$a_f = -\frac{\mu}{\left(v_\infty^+\right)^2} \tag{5}$$

where μ is the gravitational parameter of the central body. The pericenter speed and radius on the departure hyperbola are given by,

$$v_{p_f} = \sqrt{\left(v_\infty^+\right)^2 + \frac{2\mu}{r_{p_f}}} \qquad r_{p_f} = a_f(1 - e_f) \tag{6}$$

and the angular momentum magnitude and eccentricity are

$$h_f = \sqrt{\mu a_f (1 - e_f{}^2)} = r_{p_f}\ v_{p_f} \qquad e_f = \sqrt{1 - \frac{h_f}{a_f \mu}} \tag{7}$$

For the 3-impulse IG constructions, r_{p_f} will be chosen as some ratio of r_{min}, but for the 1-impulse IG r_{p_f} is determined on a case by case basis as a function of e_f. Once e_f is known the turning angle δ and the true anomaly associated with $\mathbf{v}_\infty^+$ on the departure hyperbola ν_∞^+ may be computed,

$$\delta = 2\arcsin\left(\frac{1}{e_f}\right) \tag{8}$$

$$\nu_\infty^+ = \arccos\left(\frac{-1}{e_f}\right) \tag{9}$$

The incoming hyperbolic excess velocity vector, $\hat{\mathbf{v}}_\infty^-$, is given by

$$\hat{\mathbf{v}}_\infty^- = (\cos\delta)\,\hat{\mathbf{v}}_\infty^+ + (\sin\delta)\left(\hat{\mathbf{v}}_\infty^+ \times \hat{\mathbf{h}}_f\right) \tag{10}$$

The direction of the pericenter position and velocity vectors of the hyperbola are then given for all cases as,

$$\hat{\mathbf{r}}_{p_f} = \frac{\hat{\mathbf{v}}_\infty^- - \hat{\mathbf{v}}_\infty^+}{\left\|\hat{\mathbf{v}}_\infty^- - \hat{\mathbf{v}}_\infty^+\right\|}, \qquad \hat{\mathbf{v}}_{p_f} = \frac{\hat{\mathbf{v}}_\infty^- + \hat{\mathbf{v}}_\infty^+}{\left\|\hat{\mathbf{v}}_\infty^- + \hat{\mathbf{v}}_\infty^+\right\|} \tag{11}$$

And finally, the pericenter position and velocity vectors of the hyperbola are

$$\mathbf{r}_{p_f} = r_{p_f}\ \hat{\mathbf{r}}_{p_f}, \qquad \mathbf{v}_{p_f} = v_{p_f}\ \hat{\mathbf{v}}_{p_f} \tag{12}$$

A. Single-Impulse Escape

The single injection maneuver must be made at some point along the parking orbit, and therefore the TOF is considered to be zero. There is one location on the parking orbit which minimizes the ΔV to take the spacecraft from Orbit 0 to Orbit f (the post maneuver hyperbola containing the target $\mathbf{v}_\infty^+$).

1. 1-Impulse IG Construction

The inputs to the 1-impulse IG are: $\mathbf{v}_\infty^+$, the parking orbit elements, and the state at t_0. For a single-impulse from a circular parking orbit, the $\hat{\mathbf{h}}_f^*$ unit vectors computed in Eqs. (2)-(4) are sufficiently close to the optimal and so are maintained in the construction of the IG ($\hat{\mathbf{h}}_f = \hat{\mathbf{h}}_f^*$). Ocampo and Saudemont[2] consider improvement to the IG when $e_0 \neq 0$, but otherwise this construction follows their work. The injection maneuver and its magnitude is given in Eq. (13),

$$\Delta\mathbf{v}_1 = \mathbf{v}_1^+ - \mathbf{v}_1^- \qquad \Delta V = \|\Delta\mathbf{v}_1\| \tag{13}$$

where $\mathbf{v}_1^+$ and $\mathbf{v}_1^-$ are to be determined along with the position vector, $\mathbf{r}_{\Delta v_1}$, at which the maneuver is applied, occurring at t_1 on Orbit 0 . A 1-impulse transfer targeting an example $\mathbf{v}_\infty^+$ is shown in Figure 1.

The position vector at which the departure maneuver is made, $\mathbf{r}_{\Delta v_1}$, must lie both in the plane of Orbit 0 and Orbit f. The construction of the IG, depends on whether Orbit 0 and Orbit f simply intersect or fully coincide. Hence, consider two sub-cases associated with final to initial orbit coincidence:

1. $\hat{\mathbf{h}}_0 \cdot \hat{\mathbf{v}}_\infty^+ = 0$ (orbit planes are coincident, $\hat{\mathbf{h}}_0 || \hat{\mathbf{h}}_f$). This is the trivial case, $\mathbf{r}_{\Delta v_1}$ is the pericenter position vector of the departure hyperbola,

   $$\mathbf{r}_{\Delta v_1} = r_{p_0}\ \hat{\mathbf{r}}_{p_f}$$

   The departure hyperbola and the post maneuver velocity vector $\mathbf{v}_1^+ = \mathbf{v}_{p_f}$ may then be fully defined using Eqs. (5)-(12). The velocity vector before the departure maneuver is

   $$\mathbf{v}_1^- = \sqrt{\frac{\mu}{r_{p_0}}}\ \hat{\mathbf{v}}_{p_f}$$

2. $\hat{\mathbf{h}}_0 \cdot \hat{\mathbf{v}}_\infty^+ \neq 0$ (orbit planes intersect). This is the most general case. The position vector direction where the maneuver occurs is fixed and along,

   $$\hat{\mathbf{r}}_{\Delta v_1} = \frac{\hat{\mathbf{v}}_\infty^+ \times \hat{\mathbf{h}}_f}{\left\|\hat{\mathbf{v}}_\infty^+ \times \hat{\mathbf{h}}_f\right\|} \tag{14}$$

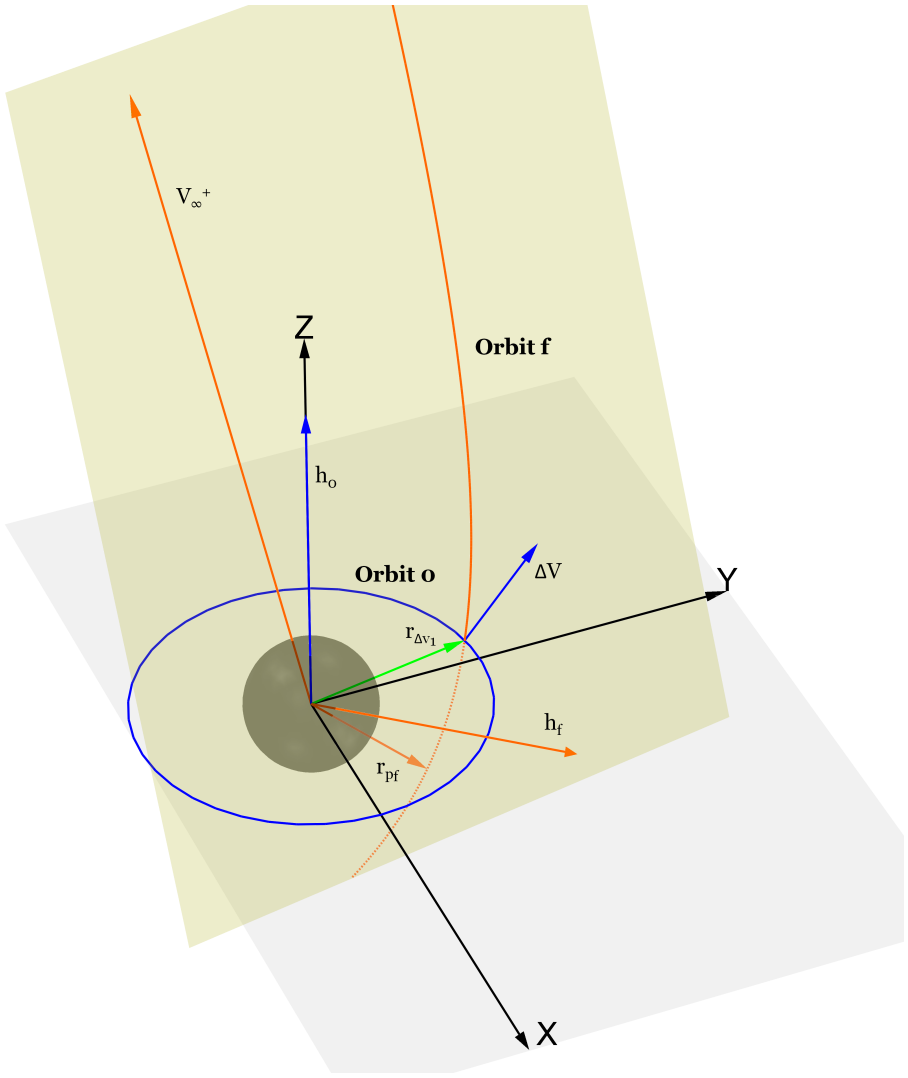

Figure 1. Sketch of 1-Impulse IG Escape (not to scale): $\delta_{rel} = 60°$, $\alpha_{rel} = 190°$, from a Circular and Equatorial Parking Orbit.

The true anomaly associated with $\mathbf{r}_{\Delta v_1}$ on Orbit 0 must be found. It is referred to as ν_{10} and is the angle between $\hat{\mathbf{r}}_{p_0}$ (the pericenter direction vector of Orbit 0) and $\hat{\mathbf{r}}_{\Delta v_1}$ that is measured positive about $\hat{\mathbf{h}}_0$ from $\hat{\mathbf{r}}_{p_0}$:

$$\nu_{10} = \left[\text{sign}\left(\hat{\mathbf{h}}_0 \cdot (\hat{\mathbf{r}}_{p_0} \times \hat{\mathbf{r}}_{\Delta v_1})\right)\right] \arccos\left(\hat{\mathbf{r}}_{p_0} \cdot \hat{\mathbf{r}}_{\Delta v_1}\right)$$

It is noted that $-\pi \leq \nu_{10} \leq \pi$ which can then be modulated to be between 0 and 2π. The magnitude of $\mathbf{r}_{\Delta v_1}$ is computed as

$$r_{\Delta v_1} = \frac{a_0\left(1 - e_0^2\right)}{1 + e_0 \cos \nu_{10}}$$

so that

$$\mathbf{r}_{\Delta v_1} = r_{\Delta v_1}\ \hat{\mathbf{r}}_{\Delta v_1}$$

The hyperbola that contains both $\mathbf{r}_{\Delta v_1}$ and $\mathbf{v}_\infty^+$ must be determined. It is observed that $\mathbf{r}_{\Delta v_1}$ is not necessarily the pericenter position vector of the departure hyperbola, and that it lies at the intersection of both orbit planes, between the pericenter vector of the hyperbola $\mathbf{r}_{p_f}$ and its outgoing asymptote.

The true anomaly of $\mathbf{r}_{\Delta v_1}$ on the hyperbola, ν_{1f}, is unknown but satisfies the polar equation,

$$r_{\Delta v_1} = \frac{a_f(1 - {e_f}^2)}{1 + e_f \cos \nu_{1f}} \tag{15}$$

The eccentricity of the departure hyperbola, e_f, is also unknown. With ν_∞^+ being the true anomaly associated with $\mathbf{v}_\infty^+$ defined in Eq. (9), and it is known that $0 \leq \nu_{1f} < \nu_\infty^+$. The angle between $\hat{\mathbf{r}}_{\Delta v_1}$ and $\hat{\mathbf{v}}_\infty^+$ is $\frac{\pi}{2}$, from Eq. (14). With

$$\nu_{1f} = \nu_\infty^+ - \frac{\pi}{2} \tag{16}$$

Equations (15), (16), and (9) are combined to obtain the system of nonlinear equations,

$$\begin{cases} r_{\Delta v_1} & = \dfrac{a_f(1-{e_f}^2)}{1+e_f \sin\nu_\infty^+} \\ \cos\nu_\infty^+ & = \left(-\dfrac{1}{e_f}\right) \end{cases} \tag{17}$$

with unknowns e_f and ν_∞^+, which has a unique solution in the ranges $1 < e_f < \infty$ and $\frac{\pi}{2} < \nu_\infty^+ < \pi$:

$$e_f = \frac{\sqrt{1+2\kappa^2+2\kappa+\sqrt{1+4\kappa}}}{\sqrt{2}\kappa} \quad \text{where } \kappa = -\frac{a_f}{r_{\Delta v_1}} \tag{18a}$$

$$\nu_\infty^+ = \arccos\left(-\frac{1}{e_f}\right) \tag{18b}$$

Then, the true anomaly on the hyperbola associated with $\mathbf{r}_{\Delta v_1}$ is computed, from Eq. (16), and with ν_∞^+ and e_f computed, the departure hyperbola elements may be computed from Eqs. (5)-(12). The post-maneuver velocity required at $\mathbf{r}_{\Delta v_1}$ is then simply[7]

$$\mathbf{v}_1^+ = \sqrt{\frac{\mu}{a_f\left(1-e_f^2\right)}}\left[(-\sin\nu_{1f})\,\hat{\mathbf{r}}_{p_f} + (e_f+\cos\nu_{1f})\,\hat{\mathbf{v}}_{p_f}\right]$$

and the pre-maneuver velocity on Orbit 0 is

$$\mathbf{v}_1^- = \sqrt{\frac{\mu}{a_0\left(1-e_0^2\right)}}\left[(-\sin\nu_{10})\,\hat{\mathbf{r}}_{p_0} + (e_0+\cos\nu_{10})\,\hat{\mathbf{v}}_{p_0}\right]$$

The required maneuver is given by Eq. (13).

The time (Δt_1) from the initial true anomaly ν_0 to ν_{10} is found by numerically solving Kepler's equation on the initial parking orbit. Some additional coasting is added to the time where the maneuver occurs (t_1), in order to ensure that t_1 will not tend below t_0 during optimization, where T_{p_0} is the time period of Orbit 0

$$t_1 = \Delta t_1 + T_{p_0}$$

This completes the IG construction for the 1-impulse escape.

2. 1-Impulse Optimization Problem

The 1-impulse optimization problem is therefore to determine the parameter vector $\mathbf{X_p}$ which minimizes $J = \|\Delta\mathbf{v}_1\|$, subject to equality ($\mathbf{C}$) and inequality ($\mathbf{D}$) constraint vectors, where

$$\mathbf{X_p} = \begin{bmatrix} \Delta\mathbf{v}_1 \\ t_1 \end{bmatrix}_{4x1} \quad \mathbf{C} = \left[\mathbf{v}_\infty^* - \mathbf{v}_\infty^+\right]_{3x1} = 0 \quad \mathbf{D} = [t_1 - t_0]_{1x1} \geq 0 \tag{19}$$

And $\mathbf{v}_\infty^*$ is the Keplerian forward propagated excess velocity vector. To compare the proximity of the IG to the optimal over a variety of input parameters (escape geometries) a non-dimensional parameter vector error X_p^{err} is introduced

$$X_p^{err} = \sqrt{\left(\frac{(\Delta\mathbf{v}_1)_{opt} - (\Delta\mathbf{v}_1)_{IG}}{(\Delta\mathbf{v}_1)_{opt}}\right)^2 + \left(\frac{(t_1)_{opt} - (t_1)_{IG}}{(t_1)_{opt}}\right)^2} \tag{20}$$

B. Time-Free 3-Impulse Escape

To achieve $\mathbf{v}_\infty^+$ from the parking orbit, a 3-impulse transfer sequence may be used, which is particularly beneficial (in terms of cost savings over the 1-impulse) when the departure orbit plane is non-coincident to the parking orbit ($\hat{\mathbf{h}}_0 \cdot \hat{\mathbf{v}}_\infty \neq 0$). When the orbit planes are coincident and $r_{min} = r_{p_0}$, the one-impulse maneuver will yield the same cost but with a much shorter TOF, and so it is defaulted to.[4] When $r_{min} \neq r_{p_0}$, the criteria for switching is generally some balance between cost savings and TOF savings. This is covered in detail in section IV-D.

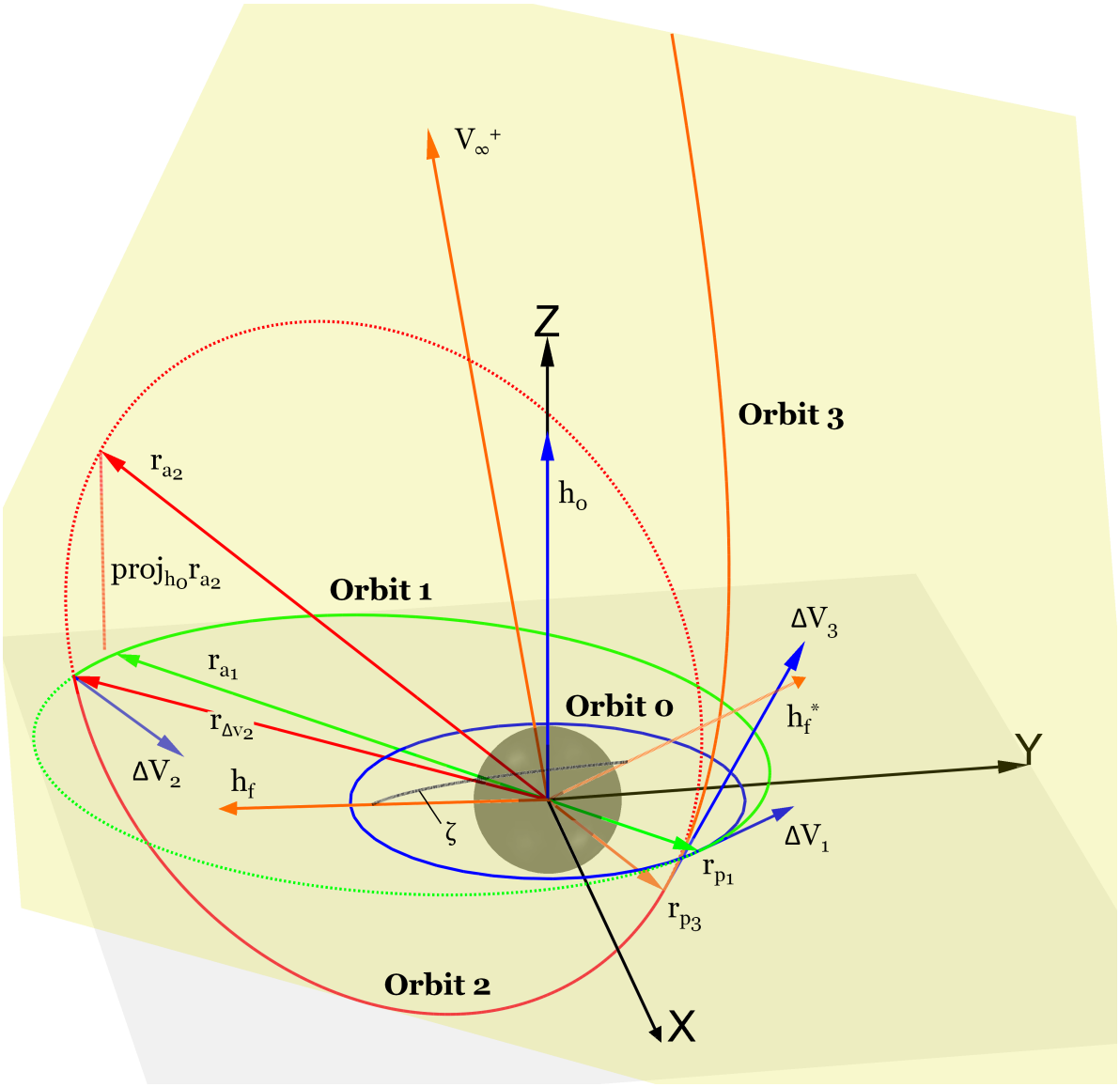

Figure 2. Sketch of 3-Impulse Time-Free IG Escape (not to scale): $\delta_{rel} = 60°$, $\alpha_{rel} = 190°$, from a Circular and Equatorial Parking Orbit.

1. *Time-Free 3-Impulse IG Construction*

The inputs to the time-free 3-impulse IG are: $\mathbf{v}_\infty^+$, r_{min}, r_{max}, the parking orbit elements, and the state at t_0. The pericenter radii of Orbits f and 2 are set equal ($r_{p_f} = r_{p_3} = r_{p_2}$)* to some ratio above r_{min}. Similarly, the apocenter radius of Orbit 1 is selected as some ratio below r_{max}. Although the optimum r_{p_2}

*For the 3-impulse escape the subscript $_3$ will be used synonymously with $_f$, since they are the same Orbit.

and r_{a_1} are known to occur at r_{min} and r_{max},[4] experimentally it has been determined that it is best to start off these limits when using a SQP method.

The impulsive maneuver vectors and the times at which they occur are determined by computing each of the intermediate orbits, which are illustrated in Figure 2:

- $\Delta\mathbf{v}_1$ is a tangential maneuver occurring at $\mathbf{r}_{p_1}$ which raises the apocenter radius of the parking orbit to that of Orbit 1.
- $\Delta\mathbf{v}_2$ occurs at the intersection of the parking orbit and departure hyperbola planes ($\mathbf{r}_{\Delta v_2}$), and includes in-plane and out-of plane components, yielding Orbit 2.
- $\Delta\mathbf{v}_3$ is an in-plane maneuver which occurs at pericenter, resulting in Orbit f.

As depicted in Figure 2, the apocenter direction of Orbit 1 ($\hat{\mathbf{r}}_{a_1}$) is chosen to be along the projection of the Orbit 2 apocenter ($\hat{\mathbf{r}}_{a_2}$) onto the parking orbit plane. This differs from that of,[2] where $\hat{\mathbf{r}}_{a_1}$ is defined along the intersection of the two planes ($\hat{\mathbf{r}}_{a_1} = \hat{\mathbf{r}}_{\Delta v_2}$), resulting in a large rotation of the apses and a poor initial guess for small δ_{rel}. This improvement is primarily responsible for IG cost reduction and increased proximity to the optimal, versus the heritage method, a result which is shown graphically in section IV-B.

If the parking orbit is coincident or normal to $\mathbf{v}_\infty^+$, then $\hat{\mathbf{h}}_f = \hat{\mathbf{h}}_f^*$ is maintained, as in the 1-impulse escape. For the general case ($0 < |\hat{\mathbf{h}}_0 \cdot \hat{\mathbf{v}}_\infty^+| < 1$), $\hat{\mathbf{h}}_f^*$ is rotated to $\hat{\mathbf{h}}_f$ by an angle ζ about the specified $\hat{\mathbf{v}}_\infty^+$ vector. Recall, that $\hat{\mathbf{h}}_f^*$ was defined in order to minimize the total plane change θ, which is defined as

$$\theta = \arccos\left(\hat{\mathbf{h}}_f^* \cdot \hat{\mathbf{h}}_0\right) \tag{21}$$

However, in the optimal, the combination of primary costs associated with the escape: plane change and apses rotation are minimized. Edelbaum states[5] that the apses rotation cost is of the order $1/\sqrt{r_{max}}$, when performed at r_{max}. But with $\hat{\mathbf{r}}_{a_1}$ selected as the projection of $\hat{\mathbf{r}}_{a_2}$ onto the parking orbit plane, $\Delta\mathbf{v}_2$ cannot occur at r_{max}. The near minimal combination of plane change and apses rotation cost, is reflected in the IG by choosing $\hat{\mathbf{r}}_{a_1}$ as the projection of $\hat{\mathbf{r}}_{a_2}$ and through the rotation of $\hat{\mathbf{h}}_f^*$ to $\hat{\mathbf{h}}_f$ by some angle ζ (a factor proportional to $1/\sqrt{r_{max}}$). Therefore, θ is increased from the minimum, which decreases the apses rotation cost. Equation (22) presents a ζ factor which has been determined to work well experimentally.

$$\zeta = \left[\text{sign}\left(\hat{\mathbf{h}}_0 \cdot \hat{\mathbf{v}}_\infty^+\right)\right]\left(\frac{\sin\theta}{\sin\nu_\infty^+}\right)\left(\frac{2}{\sqrt{r_{max}/r_{p_0}}}\right) \tag{22}$$

Where ν_∞^+ is the true anomaly associated with $\hat{\mathbf{v}}_\infty^+$ on the departure hyperbola defined in Eq. (9). Finally, an Euler rotation can be utilized to compute the rotated $\hat{\mathbf{h}}_f$:

$$\hat{\mathbf{h}}_f = (\cos\zeta)\,\hat{\mathbf{h}}_f^* + (1-\cos\zeta)\left(\hat{\mathbf{v}}_\infty^+ \cdot \hat{\mathbf{h}}_f^*\right)\hat{\mathbf{v}}_\infty^+ - \sin\zeta\left(\hat{\mathbf{v}}_\infty^+ \times \hat{\mathbf{h}}_f^*\right) \tag{23}$$

With $\hat{\mathbf{h}}_f$ selected Orbit f may be fully defined using Eqs. (5)-(12). In order to determine the pre/post maneuver velocities, Orbits 1 and 2 must be defined. The line of apses for Orbit 2 is aligned with $\hat{\mathbf{r}}_{p_f}$ so that

$$\hat{\mathbf{r}}_{p_2} = \hat{\mathbf{r}}_{p_f} \qquad \hat{\mathbf{r}}_{a_2} = -\hat{\mathbf{r}}_{p_2} \tag{24}$$

The plane change maneuver $\Delta\mathbf{v}_2$ will not necessarily occur at the apocenter of Orbit 2, since it must occur at the intersection of the planes. In any case, the planes of Orbit 0 and Orbit 1 coincide, as do those of Orbit 2 and Orbit f. The location of the second maneuver is called $\mathbf{r}_{\Delta v_2}$, and it is determined based on the three cases of final/initial orbit coincidence. The unit vectors $\hat{\mathbf{r}}_{a_1}$ and $\hat{\mathbf{r}}_{\Delta v_2}$, and the true anomaly of $\mathbf{r}_{\Delta v_2}$ on Orbit 1 (ν_{21}) and on Orbit 2 (ν_{22}) are also computed based on these three cases:

1. $|\hat{\mathbf{h}}_0 \cdot \hat{\mathbf{v}}_\infty^+| = 0$ (orbit planes are coincident)

   This case is trivial, let

$$\hat{\mathbf{r}}_{a_1} = \hat{\mathbf{r}}_{a_2} = -\hat{\mathbf{r}}_{p_1} \qquad \hat{\mathbf{r}}_{\Delta v_2} = \hat{\mathbf{r}}_{a_1} = -\hat{\mathbf{r}}_{p_1} \tag{25}$$

$$\nu_{21} = \pi \qquad \nu_{22} = \pi \tag{26}$$

2. $|\hat{\mathbf{h}}_0 \cdot \hat{\mathbf{v}}_\infty^+| = 1$ (orbit planes are orthogonal)

   Here, $\hat{\mathbf{r}}_{a_1} = \hat{\mathbf{r}}_{\Delta v_2}$ and defined through the projection

$$\hat{\mathbf{r}}_{\Delta v_2} = \hat{\mathbf{r}}_{a_1} = -\hat{\mathbf{r}}_{p_1} = \frac{(\hat{\mathbf{r}}_{a_2} \cdot \hat{\mathbf{r}}_{p_0})\,\hat{\mathbf{r}}_{p_0} + (\hat{\mathbf{r}}_{a_2} \cdot \hat{\mathbf{v}}_{p_0})\,\hat{\mathbf{v}}_{p_0}}{\|(\hat{\mathbf{r}}_{a_2} \cdot \hat{\mathbf{r}}_{p_0})\,\hat{\mathbf{r}}_{p_0} + (\hat{\mathbf{r}}_{a_2} \cdot \hat{\mathbf{v}}_{p_0})\,\hat{\mathbf{v}}_{p_0}\|} \tag{27}$$

$$\nu_{21} = \pi \qquad \Delta\nu_{22} = \arccos(\hat{\mathbf{r}}_{a_2} \cdot \hat{\mathbf{r}}_{\Delta v_2}) \qquad \nu_{22} = \pi + \Delta\nu_{22} \tag{28}$$

3. $0 < |\hat{\mathbf{h}}_0 \cdot \hat{\mathbf{v}}_\infty^+| < 1$ (general case)

   The apocenter direction for Orbit 1 $\hat{\mathbf{r}}_{a_1}$ is again defined through the projection

$$\hat{\mathbf{r}}_{a_1} = -\hat{\mathbf{r}}_{p_1} = \frac{(\hat{\mathbf{r}}_{a_2} \cdot \hat{\mathbf{r}}_{p_0})\,\hat{\mathbf{r}}_{p_0} + (\hat{\mathbf{r}}_{a_2} \cdot \hat{\mathbf{v}}_{p_0})\,\hat{\mathbf{v}}_{p_0}}{\|(\hat{\mathbf{r}}_{a_2} \cdot \hat{\mathbf{r}}_{p_0})\,\hat{\mathbf{r}}_{p_0} + (\hat{\mathbf{r}}_{a_2} \cdot \hat{\mathbf{v}}_{p_0})\,\hat{\mathbf{v}}_{p_0}\|} \tag{29}$$

   but the location of the 2nd maneuver must be located at the intersection of the two planes ($\hat{\mathbf{r}}_{a_1} \neq \hat{\mathbf{r}}_{\Delta v_2}$),

$$\hat{\mathbf{r}}_{\Delta v_2} = \left[\text{sign}\left(\hat{\mathbf{h}}_0 \cdot \hat{\mathbf{v}}_\infty^+\right)\right] \frac{\left(\hat{\mathbf{h}}_f \times \hat{\mathbf{h}}_0\right)}{\left\|\left(\hat{\mathbf{h}}_f \times \hat{\mathbf{h}}_0\right)\right\|} \tag{30}$$

$$\Delta\nu_{21} = \arccos(\hat{\mathbf{r}}_{a_1} \cdot \hat{\mathbf{r}}_{\Delta v_2}) \qquad \nu_{21} = \pi + \Delta\nu_{21} \tag{31}$$

$$\Delta\nu_{22} = \arccos(\hat{\mathbf{r}}_{a_2} \cdot \hat{\mathbf{r}}_{\Delta v_2}) \qquad \nu_{22} = \pi + \Delta\nu_{22} \tag{32}$$

It should be noted that both $\Delta\nu_{21}$ and $\Delta\nu_{22}$ are between 0 and π, and therefore

$$\pi \;\leq \nu_{21} \;\leq\; 2\pi \qquad \pi \leq \nu_{22} \;\leq\; 2\pi$$

With $\hat{\mathbf{r}}_{a_1}$ defined and r_{a_1} specified as some ratio of r_{max}, the apocenter radius vector of Orbit 1 is

$$\mathbf{r}_{a_1} = r_{a_1}\;\hat{\mathbf{r}}_{a_1}$$

The pericenter vector of Orbit 1 can now be computed, which is also where the first maneuver $\Delta\mathbf{v}_1$ is selected to occur (transitioning from Orbit 0 to Orbit 1). The magnitude of $\mathbf{r}_{p_1}$ is required to lie on Orbit 0, so let ν_{10} be the true anomaly associated with $\mathbf{r}_{p_1}$ on Orbit 0, defined based on the following three cases:

1. $\hat{\mathbf{r}}_{p_0} \cdot \hat{\mathbf{r}}_{p_1} = 1$

$$\nu_{10} = 0 \tag{33}$$

2. $\hat{\mathbf{r}}_{p_0} \cdot \hat{\mathbf{r}}_{p_1} = -1$

$$\nu_{10} = \pi \tag{34}$$

3. $|\hat{\mathbf{r}}_{p_0} \cdot \hat{\mathbf{r}}_{p_1}| \neq 1$

$$\nu_{10} = \left[\text{sign}\left(\hat{\mathbf{h}}_0 \cdot (\hat{\mathbf{r}}_{p_0} \times \hat{\mathbf{r}}_{p_1})\right)\right] \arccos(\hat{\mathbf{r}}_{p_0} \cdot \hat{\mathbf{r}}_{p_1}) \tag{35}$$

It is noted that $-\pi \leq \nu_{10} \leq \pi$ so that ν_{10} may be modulated to be between 0 and 2π. The magnitude of $\mathbf{r}_{p_1}$ must then satisfy the polar equation for a conic section,

$$r_{p_1} = \frac{a_0\left(1 - e_0^2\right)}{1 + e_0 \cos\nu_{10}}$$

so that

$$\mathbf{r}_{p_1} = \mathbf{r}_{\Delta v_1} = r_{p_1}\;\hat{\mathbf{r}}_{p_1}$$

The Orbit 1 semi-major axis and eccentricity are then

$$a_1 = \frac{r_{a_1} + r_{p_1}}{2} \qquad e_1 = \frac{r_{a_1} - r_{p_1}}{r_{a_1} + r_{p_1}}$$

With Orbit 1 fully defined and ν_{21} known, the radial magnitude where the 2nd maneuver occurs may be computed from the polar equation of a conic section,

$$r_{\Delta v_2} = \frac{a_1\left(1-e_1^2\right)}{1+e_1\cos\nu_{21}}$$

And verifying the polar equation of a conic section for $r_{\Delta v_2}$ on Orbit 2 yields e_2 and a_2

$$e_2 = \frac{r_{\Delta v_2} - r_{p_2}}{r_{\Delta v_2}\cos\Delta\nu_{22} + r_{p_2}} \qquad a_2 = \frac{r_{p_2}}{1-e_2}$$

Recall that $r_{p_2} = r_{p_f}$, and is known as some ratio of r_{min}. Orbits 1 and 2 are now completely defined and the velocity vectors before and after each maneuver may be computed.

Regarding the first maneuver, $\Delta\mathbf{v}_1$, the speed at pericenter on Orbit 1 is computed from

$$v_{p_1} = \sqrt{\mu\left(\frac{2}{r_{p_1}} - \frac{1}{a_1}\right)} \tag{36}$$

so that

$$\mathbf{v}_1^+ = v_{p_1}\hat{\mathbf{v}}_{p_1} \qquad \hat{\mathbf{v}}_{p_1} = \hat{\mathbf{h}}_0 \times \hat{\mathbf{r}}_{p_1} \tag{37}$$

and

$$\mathbf{v}_1^- = \sqrt{\frac{\mu}{a_0\left(1-e_0^2\right)}}\left[\left(-\sin\nu_{10}\right)\hat{\mathbf{r}}_{p_0} + \left(e_0+\cos\nu_{10}\right)\hat{\mathbf{v}}_{p_0}\right] \tag{38}$$

Finally

$$\Delta\mathbf{v}_1 = \mathbf{v}_1^+ - \mathbf{v}_1^- \tag{39}$$

For the 2nd maneuver, $\Delta\mathbf{v}_2$, the velocity on Orbit 1 at $\mathbf{r}_{\Delta v_2}$ is given by

$$\mathbf{v}_2^- = \sqrt{\frac{\mu}{a_1\left(1-e_1^2\right)}}\left[\left(-\sin\nu_{21}\right)\hat{\mathbf{r}}_{p_1} + \left(e_1+\cos\nu_{21}\right)\hat{\mathbf{v}}_{p_1}\right] \tag{40}$$

And the velocity on Orbit 2 at $\mathbf{r}_{\Delta v_2}$ is given by

$$\mathbf{v}_2^+ = \sqrt{\frac{\mu}{a_2\left(1-e_2^2\right)}}\left[\left(-\sin\nu_{22}\right)\hat{\mathbf{r}}_{p_f} + \left(e_2+\cos\nu_{22}\right)\hat{\mathbf{v}}_{p_f}\right] \tag{41}$$

Finally

$$\Delta\mathbf{v}_2 = \mathbf{v}_2^+ - \mathbf{v}_2^- \tag{42}$$

Regarding the third maneuver, $\Delta\mathbf{v}_3$, the speed at pericenter on Orbit 2 is computed from

$$v_{p_2} = \sqrt{\mu\left(\frac{2}{r_{p_2}} - \frac{1}{a_2}\right)} \tag{43}$$

Let

$$\mathbf{v}_3^+ = \mathbf{v}_{p_f} \qquad \text{and} \qquad \mathbf{v}_3^- = v_{p_2}\mathbf{v}_{p_f} \tag{44}$$

Where $\mathbf{v}_{p_f}$ is given by Eq. (11), and finally

$$\Delta\mathbf{v}_3 = \mathbf{v}_3^+ - \mathbf{v}_3^- \tag{45}$$

The times between maneuvers are found numerically via Kepler's equation: Δt_1 from ν_0 to ν_{10} on Orbit 0, Δt_2 from ν_{10} to ν_{21} on Orbit 1, and Δt_3 from ν_{22} to 0 on Orbit 2. As in the 1-impulse case additional costing is added to t_1 such that,

$$t_1 = \Delta t_1 + T_{p_0} \qquad t_2 = \Delta t_2 + t_1 \qquad t_3 = \Delta t_3 + t_2$$

This completes the 3-impulse time-free IG construction.

2. Time-Free 3-Impulse Optimization Problem

The scalar performance index J is

$$J = \Delta V = \|\Delta \mathbf{v}_1\| + \|\Delta \mathbf{v}_2\| + \|\Delta \mathbf{v}_3\| \tag{46}$$

The parameter vector $\mathbf{X_p}$ includes the maneuver vectors and the times at which they occur. Additional inequality constraints must be introduced to ensure the pericenter and apocenter limits are not exceeded. In general, since $\Delta\mathbf{v_3}$ is an energy increasing maneuver $r_{p_3} > r_{p_2}$ in the optimal and so r_{p_2} is the only pericenter radii constrained. The 3-impulse time-free optimization problem is stated as,

$$\mathbf{X_p} = \begin{bmatrix} \Delta\mathbf{v}_1 \\ \Delta\mathbf{v}_2 \\ \Delta\mathbf{v}_3 \\ t_1 \\ t_2 \\ t_3 \end{bmatrix}_{12x1} \qquad \mathbf{C} = \left[\mathbf{v}_\infty^* - \mathbf{v}_\infty^+\right]_{3x1} = 0 \quad \mathbf{D} = \begin{bmatrix} t_1 - t_0 \\ t_2 - t_1 \\ t_3 - t_2 \\ r_{p_2} - r_{min} \\ r_{p_1} - r_{min} \\ r_{max} - r_{a_1} \end{bmatrix}_{6x1} \geq 0 \tag{47}$$

And $\mathbf{v}_\infty^*$ is the Keplerian forward propagated excess velocity vector. Once again to compare the proximity of the IG to the optimal a non-dimensional parameter vector error is introduced as

$$X_p^{err} = \sqrt{\left(\frac{\Delta\mathbf{V}_{opt} - \Delta\mathbf{V}_{IG}}{\|\Delta\mathbf{V}_{opt}\|}\right)^2 + \left(\frac{(t_1)_{opt} - (t_1)_{IG}}{(t_1)_{opt}}\right)^2 + \left(\frac{(t_2)_{opt} - (t_2)_{IG}}{(t_2)_{opt}}\right)^2 + \left(\frac{(t_3)_{opt} - (t_3)_{IG}}{(t_3)_{opt}}\right)^2} \tag{48}$$

Where,

$$\Delta\mathbf{V} = \begin{bmatrix} \Delta\mathbf{v}_1 \\ \Delta\mathbf{v}_2 \\ \Delta\mathbf{v}_3 \end{bmatrix}_{9x1} \tag{49}$$

3. Alternate Time-Free 3-Impulse Optimization Problem

The size of the optimization problem can be reduced by explicitly solving for the $\Delta\mathbf{v}_3$ necessary to achieve the specified $\mathbf{v}_\infty^+$, thereby eliminating $\Delta\mathbf{v}_3$ from $\mathbf{X_p}$ and eliminating $\mathbf{C}$ entirely.

t_1, t_2, t_3, $\Delta\mathbf{v}_1$, and $\Delta\mathbf{v}_2$ are changing during optimization, but $\mathbf{v}_3^-$ and $\mathbf{r}_{\Delta v_3}$ can be computed from these parameters via forward Keplerian propagation. a_f remains constant during optimization as given in Eq. (5), but the departure hyperbola eccentricity, e_f, and the true anomaly of $\Delta\mathbf{v}_3$ on Orbit f, ν_{3f}, will change. However, $r_{\Delta v_3}$ must satisfy the polar equation of a conic section on the departure hyperbola,

$$r_{\Delta v_3} = \frac{a_f\left(1 - e_f^2\right)}{1 + e_f \cos\nu_{3f}} \tag{50}$$

The angle between $\hat{\mathbf{r}}_{\Delta v_3}$ and $\hat{\mathbf{v}}_\infty^+$, $\Delta\nu_{3f}$ is defined as,

$$\Delta\nu_{3f} = \arccos\left(\hat{\mathbf{r}}_{\Delta v_3} \cdot \hat{\mathbf{v}}_\infty^+\right) \tag{51}$$

And looking at the escape orbit plane, ν_{3f} is related to $\Delta\nu_{3f}$ and ν_∞^+ by

$$\nu_{3f} = \nu_\infty^+ - \Delta\nu_{3f} \tag{52}$$

Where ν_∞^+ is a function of e_f from Eq. (9). Since $\Delta\nu_{3f}$ is known from Eq. (51), Eqs. (50), (52), and (9) can be combined. Solving for e_f yields Eq. (53) which has a unique solution in the range $1 < e_f < \infty$.

$$e_f = \frac{\sqrt{\sin^2\Delta\nu_{3f} + 2\kappa^2 + 2\kappa(1 - \cos\Delta\nu_{3f}) + \sin\Delta\nu_{3f}\sqrt{\sin^2\Delta\nu_{3f} + 4\kappa(1 - \cos\Delta\nu_{3f})}}}{\sqrt{2}\kappa} \tag{53}$$

Where,

$$\kappa = -\frac{a_f}{r_{\Delta v_3}} \tag{54}$$

With e_f known, ν_∞^+ and ν_{3f} can be computed using Eqs. (9) and (52), respectively. The departure hyperbola may then be fully defined using Eqs. (6)-(12). All that remains is to determine the $\mathbf{v}_3^+$ necessary to achieve the specified $\mathbf{v}_\infty^+$, which is given simply as

$$\mathbf{v}_3^+ = \sqrt{\frac{\mu}{a_f\left(1-e_f^2\right)}}\left[(-\sin\nu_{3f})\,\hat{\mathbf{r}}_{p_f} + (e_f+\cos\nu_{3f})\,\hat{\mathbf{v}}_{p_f}\right] \tag{55}$$

Since $\mathbf{v}_3^-$ is known from forward Keplerian propagation, the final maneuver is known

$$\Delta\mathbf{v}_3 = \mathbf{v}_3^+ - \mathbf{v}_3^- \tag{56}$$

An alternate optimization problem may be constructed, referred to as 3-impulse time-free without $\Delta\mathbf{v}_3$. The performance index J and inequality constraint vector $\mathbf{D}$ are the same as given in Eqs. (46)-(47), but there is no longer an equality constraint vector $\mathbf{C}$ (it is satisfied directly) and the new $\mathbf{X_p}$ is given by,

$$\mathbf{X_p} = \begin{bmatrix} \Delta\mathbf{v}_1 \\ \Delta\mathbf{v}_2 \\ t_1 \\ t_2 \\ t_3 \end{bmatrix}_{9x1} \tag{57}$$

The non-dimensional parameter vector error (X_p^{err}) is the same as that given in Eq. (48) but with $\Delta\mathbf{V}$ given by Eq. (58)

$$\Delta\mathbf{V} = \begin{bmatrix} \Delta\mathbf{v}_1 \\ \Delta\mathbf{v}_2 \end{bmatrix}_{6x1} \tag{58}$$

C. Time-Fixed 3-Impulse Escape

The following construction is useful in that it allows for quick cost assessments for particular escape geometries as a function of the TOF. These TOF specific, feasible escapes, may still be optimized using parameter optimization techniques as opposed to primer vector theory. For this analysis, the initial state on the parking orbit is considered arbitrary (i.e. $t_1 = t_0$ and $\nu_0 = \nu_{10}$).

1. Time-Fixed 3-Impulse IG Construction

The inputs required for the generation of a time-fixed 3-impulse IG are: $\mathbf{v}_\infty^+$, r_{min}, TOF, the parking orbit elements, and the initial epoch ($t_0 = t_1$).[†] When the escape time ($TOF = t_3 - t_1$) is specified, the relative energy and lines of apses for Orbits 1 and 2 are not arbitrary (as in the 3-impulse time-free IG method), but are related and constrained by the TOF. In order to handle this and because this construction is meant to provide rough estimates, the following strategy is adopted:

- $\hat{\mathbf{h}}_f$ is maintained as defined in Eqs. (2)-(4) based on the three cases of initial and final orbit coincidence. This is similar to the 1-impulse IG, and in contrast to the rotation by the angle ζ as in the 3-impulse time-free IG.
- Orbit 1 is defined with $\hat{\mathbf{r}}_{a_1}$ along the projection of $-\hat{\mathbf{r}}_{p_f}$ onto the parking orbit plane (this is identical to the 3-impulse time-free, except $\hat{\mathbf{r}}_{a_2}$ is not necessarily the same as $-\hat{\mathbf{r}}_{p_f}$), and Orbit 1 is given a time period equal to the escape time ($T_{p_1} = TOF$). $\Delta\mathbf{v}_1$ is purely in-plane and occurs at the pericenter of Orbit 1, such that the planes of Orbit 0 and Orbit 1 coincide.
- In the case of fully coincident orbits ($|\hat{\mathbf{h}}_0 \cdot \hat{\mathbf{v}}_\infty^+| = 0$), Orbits 2 and f are allowed to coincide ($\mathbf{r}_{p_2} = \mathbf{r}_{p_f}$ and $\hat{\mathbf{h}}_2 = \hat{\mathbf{h}}_f$) but with pericenter magnitude ($r_{p_2} = r_{p_f}$) such that $\Delta\mathbf{v}_3$ occurs at $\mathbf{r}_{p_f}$ at time $t_3 = TOF + t_1$.

[†] r_{max} is no longer an input since the TOF, and therefore the size of the intermediate orbits, is being constrained directly.

- For non-coincident orbits, the orientation and energy of Orbit 2 are determined such that $\Delta\mathbf{v}_3$ occurs at $\mathbf{r}_{p_f}$ at time $t_3 = TOF + t_1$, causing Orbits 2 and f to not coincide ($\mathbf{r}_{p_2} \neq \mathbf{r}_{p_f}$ and $\hat{\mathbf{h}}_2 \neq \hat{\mathbf{h}}_f$).

As in the time-free case, $\Delta\mathbf{v}_2$ occurs at the intersection of Orbit 0 and Orbit f resulting in Orbit 2, which may or may not coincide with the plane of Orbit f. With the exception of the Orbit 2 orientation and the $\hat{\mathbf{h}}_f$ selection, the time-fixed 3-impulse IG follows a very similar construction to the time-free case illustrated in Figure 2. The following quantities are computed using the time-free IG Eqs. (24)-(35):

$$\hat{\mathbf{r}}_{p_1} = \hat{\mathbf{r}}_{\Delta v_1} = -\hat{\mathbf{r}}_{a_1} \ , \ \hat{\mathbf{r}}_{\Delta v_2} \ , \ \hat{\mathbf{r}}_{p_3} = \hat{\mathbf{r}}_{p_f} \ , \ \nu_{10} \ , \text{ and } \nu_{21}$$

a_1 is then computed such that Orbit 1 has time-period equal to the TOF

$$a_1 = \left(\mu \left(\frac{TOF}{2\pi} \right)^2 \right)^{\frac{1}{3}}$$

Once r_{p_f} is defined and Orbit f is computed, Orbit 1 can be fully defined along with the locations of the 1st and 2nd maneuvers, demonstrated in Eqs. (59)-(61). Also, the velocity vectors before and after the first maneuver (and therefore $\Delta\mathbf{v}_1$) may be computed using Eqs. (36)-(39).

$$r_{p_1} = r_{\Delta v_1} = \frac{a_0\left(1 - e_0^2\right)}{1 + e_0 \cos\ \nu_{10}} \qquad e_1 = 1 - \frac{r_{p_1}}{a_1} \tag{59}$$

$$r_{a_1} = a_1\left(1 + e_1\right) \qquad r_{\Delta v_2} = \frac{a_1\left(1 - e_1^2\right)}{1 + e_1 \cos\ \nu_{21}} \tag{60}$$

$$\mathbf{r}_{p_1} = \mathbf{r}_{\Delta v_1} = r_{p_1}\hat{\mathbf{r}}_{p_1} \qquad \mathbf{r}_{\Delta v_2} = r_{\Delta v_2}\hat{\mathbf{r}}_{\Delta v_2} \tag{61}$$

At this point all that remains is to define: the ratio of r_{p_f} to r_{min}, Orbit 2, and the time at which the 2nd maneuver occurs t_2. This is done on the basis of the now familiar cases of initial and final orbit coincidence:

1. $|\hat{\mathbf{h}}_0 \cdot \hat{\mathbf{v}}_\infty^+| = 0$ (orbit planes are coincident)

   As defined previously this case provides that $\mathbf{r}_{\Delta v_2} = \mathbf{r}_{a_1} = \mathbf{r}_{a_2}$ and all orbits are coincident. r_{p_f} must be determined so that the final maneuver occurs at $\mathbf{r}_{p_f}$ at the correct time. Since the 2nd maneuver occurs at the shared apocenter of Orbits 1 and 2, t_2 is simply

   $$t_2 = \frac{TOF}{2}$$

   Recalling the assumption that $r_{min} \leq r_{p_0}$, and since $r_{a_2} = r_{a_1}$, the only possible solution is if:

   $$r_{p_f} = r_{p_2} = r_{p_1} = r_{p_0}$$

   With r_{p_f} and $\hat{\mathbf{h}}_f$ known, Orbit f may be fully determined using Eqs. (5)-(12). It should be noted that, $a_1 = a_2$ and $e_1 = e_2$ (Orbit 1 is the same as Orbit 2), and therefore the IG $\Delta\mathbf{v}_2$ is zero. Orbit 1 and the locations of maneuvers 1 and 2 are then determined as outlined above, in Eqs. (59)-(61). The 1st and 3rd maneuvers are computed using Eqs. (36)-(39) and Eqs. (43)-(45), respectively.

2. $|\hat{\mathbf{h}}_0 \cdot \hat{\mathbf{v}}_\infty^+| \neq 0$

   In this general case, a solution to Lambert's problem is found in order to determine the necessary arc (specifically $\mathbf{v}_2^+$ and $\mathbf{v}_3^-$) transversing $\mathbf{r}_{\Delta v_2}$ to $\mathbf{r}_{p_f}$ in the time $t_3 - t_2$. This yields Orbit 2 as well as places the final maneuver at $\mathbf{r}_{p_f}$; however, Orbits 2 and f will not be coplanar. First, the pericenter radius of the departure hyperbola r_{p_f} is defined as some ratio of r_{min} (as in the time-free IG) and Orbit f is determined using Eqs. (5)-(12). Next, t_2 is found by solving Kepler's equation along Orbit 1 from $\mathbf{r}_{p_1}$ to $\mathbf{r}_{\Delta v_2}$, since ν_{21} is known. Also, since $\nu_{21} \geq \pi$ it is known that

   $$t_2 \geq \frac{TOF}{2}$$

With $\mathbf{v}_2^+$ and $\mathbf{r}_{\Delta v_2}$ known, the Orbit 2 elements (a_2 and e_2) may be computed as follows where ϵ_2 and h_2 are the energy and angular momentum magnitude of Orbit 2, respectively

$$\epsilon_2 = \frac{\|\mathbf{v}_2^+\|^2}{2} - \frac{\mu}{r_{\Delta v_2}} \qquad h_2 = \|\mathbf{r}_{\Delta v2} \times \mathbf{v}_2^+\|$$

$$a_2 = \frac{-\mu}{2\epsilon_2} \qquad e_2 = \sqrt{1 + \frac{2\epsilon_2 h_2^2}{\mu^2}}$$

The only remaining unknown velocities are $\mathbf{v}_2^-$ and $\mathbf{v}_3^+$, but $\mathbf{v}_2^-$ may be computed using Eq. (40), and $\mathbf{v}_3^+$ is the pericenter velocity on Orbit f derived in Eqs. (5)-(12). All maneuver vectors and the times at which they occur are now defined, and therefore the time-fixed 3-impulse IG is complete.

2. Time-Fixed 3-Impulse Optimization Problem

J and $\mathbf{C}$ are identical to the time-free optimization problem defined in Eq. (46) and Eq. (47), but $\mathbf{X_p}$ and $\mathbf{D}$ are different and given by

$$\mathbf{X_p} = \begin{bmatrix} \Delta\mathbf{v}_1 \\ \Delta\mathbf{v}_2 \\ \Delta\mathbf{v}_3 \\ t_2 \\ \nu_{10} \end{bmatrix}_{11x1} \qquad \mathbf{D} = \begin{bmatrix} t_2 - t_1 \\ t_3 - t_2 \\ r_{p_2} - r_{min} \\ r_{p_1} - r_{min} \end{bmatrix}_{4x1} \geq 0 \tag{62}$$

The number of parameters is reduced by 1, whereas the number of inequality constraints is reduced by 2, compared with the time-free problem. The extra inequality constraint lost is due to allowing $t_1 = t_0$, and therefore ignoring any coasting from ν_0 to ν_{10}. The non-dimensional parameter vector error for the time-fixed problem is given by Eq. (63).

$$X_p^{err} = \sqrt{\left(\frac{\Delta\mathbf{V}_{opt} - \Delta\mathbf{V}_{IG}}{\|\Delta\mathbf{V}_{opt}\|}\right)^2 + \left(\frac{(t_2)_{opt} - (t_2)_{IG}}{(t_2)_{opt}}\right)^2 + \left(\frac{(\nu_{10})_{opt} - (\nu_{10})_{IG}}{(\nu_{10})_{opt}}\right)^2} \tag{63}$$

Where, $\mathbf{\Delta V}$ is as given in Eq. (49).

IV. Results

The readily available SQP based *VF13ad* algorithm was used in solving each optimization problem, with convergence defined by the inequality Eqs. (64)-(65), where ϵ is a user supplied convergence tolerance.[‡]

$$\left|\frac{\partial J}{\partial \mathbf{X_p}}\ \Delta\mathbf{X_p}\right| < \epsilon \tag{64}$$

And

$$\mathbf{C}_i < \epsilon \qquad \text{for i} = 1 : \text{total number of equality constraints} \tag{65}$$

The figures that follow (unless otherwise noted) were generated using $\epsilon = 10^{-8}$, and with input parameter ranges derived from typical trans-Earth injection (TEI) targets from the Moon ($\mu = \mu_{Moon}$).[6] The non-dimensional (except r_{p_0}) input parameter ranges and step-sizes used are provided in Table 1. The parameters are presented in the order in which they are looped during the scan, with v_∞^+/v_{p_0} being the outermost loop and δ_{rel} being the innermost. Of course, for the 1-impulse escape, both r_{max} and r_{min} are ignorable.

Input Parameter	Min. Value	Max. Value	Step Size
v_∞^+/v_{p_0}	0.5404	0.8106	0.1351
r_{min}/r_{p_0}	0.8213	0.9553	0.0670
r_{max}/r_{p_0}	7.8786	13.2402	1.3401
δ_{rel}	-90°	90°	5°
r_{p_0}	2238.1 km	2238.1 km	0

Table 1. Summary of TEI Derived Input Parameter Scan Used to Generate Results

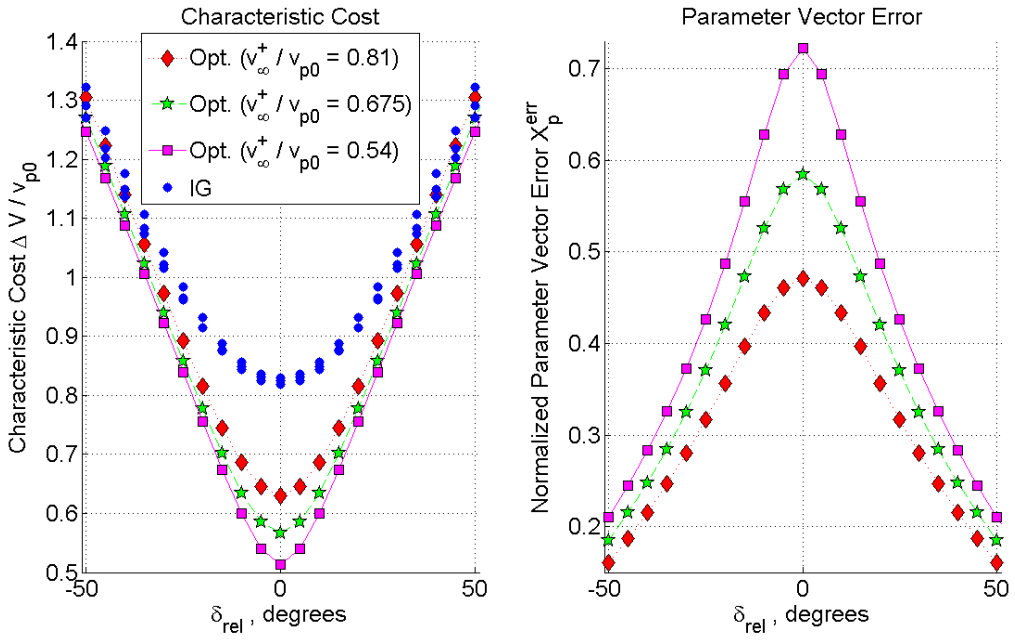

Figure 3. 1-Impulse IG and Optimal Characteristic Costs and Parameter Vector Errors vs. δ_{rel} over the Range Provided in Table 1.

A. Single-Impulse Escape Results

Over the range of inputs specified in Table 1, Figure 3 shows the IG vs. optimal characteristic ΔV, and the parameter vector error (X_p^{err}) as defined in Eq. (20).[§]

The greatest error between IG and optimal is exhibited at low δ_{rel}, and the IG becomes practically indistinguishable from the optimal at high δ_{rel} until becoming virtually zero at $\delta_{rel} = 90°$. Also, the IG most closely reflects the optimal at high characteristic escape velocities, with greater error when v_∞^+/v_{p_0} is small. As expected, the total cost increases with increasing v_∞^+/v_{p_0} and rapidly with increasing δ_{rel}.

B. Time-Free 3-Impulse Escape Results

Although, only local optima can be assured, confidence that these optima are in fact global can be achieved by providing lower quality initial guesses and ensuring that the same optimal solutions are converged upon. Identical optimal solutions were reached experimentally when the ratios of $r_{p_2} = r_{p_3} = r_{p_f}$ and r_{a_1} to the limits r_{min} and r_{max}, were varied from 0.9 to 0.5 and 1.1 to 1.5, respectively. In the following results $r_{a_1} = 0.9$ (r_{max}) and $r_{p_3} = 1.1$ (r_{min}) were used, since they are near enough to the optimal but substantially off the boundary so as to not hinder the numerical method, as determined experimentally.

[‡]For practical reasons the parameter vector, the constraints, and the cost are scaled to be near unity and much effort must be devoted to tuning these scaling factors and perturbation step sizes when optimizing, the details of which are omitted.

[§]The range of δ_{rel} shown in Figure 3 is limited because the curves converge at high $|\delta_{rel}|$

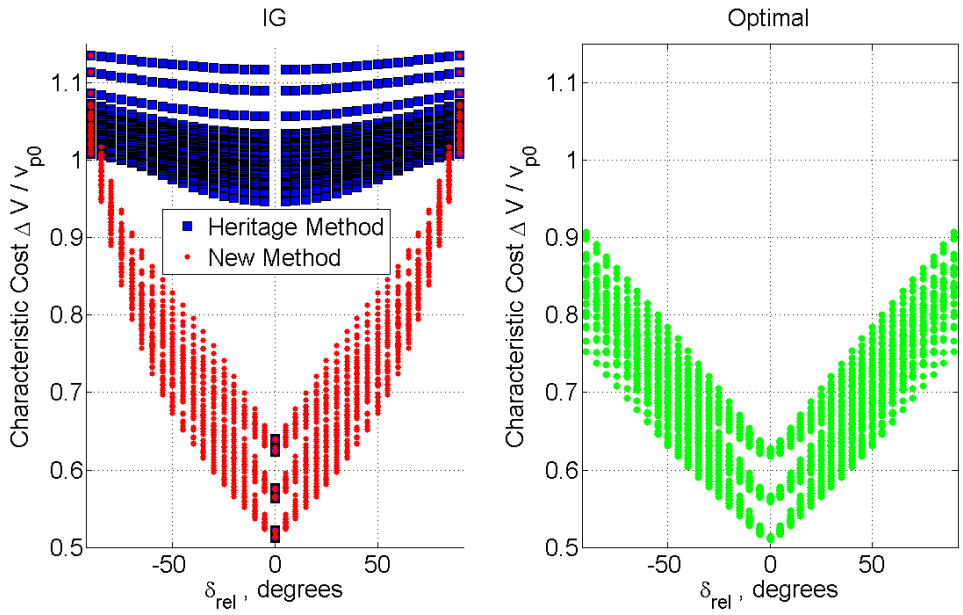

Figure 4. Total Characteristic Cost Comparison of Heritage IG, Improved IG, and Optimal vs. δ_{rel} over the Range Provided in Table 1.

The reduction in total characteristic ΔV and greater proximity to the optimal, over the range given in Table 1, compared with the heritage method,[2] is shown in Figures 4 and 5. The improved IG method therefore provides solutions much closer to the optimal as evidenced by a lower $\Delta V/v_{p_0}$ and lower X_p^{err} as defined in Eq. (48). At $\delta_{rel} = 0°$ the heritage and improved IG are identical and very close to the optimal, but as $|\delta_{rel}|$ is increased incrementally from zero a large jump in the heritage method ΔV results. This caused problems with convergence, which the new IG does not exhibit because of its closer proximity to the optimal. The considerable reduction in X_p^{err} as illustrated in Figure 5, particularly at low δ_{rel} was the major achievement of the new IG construction.

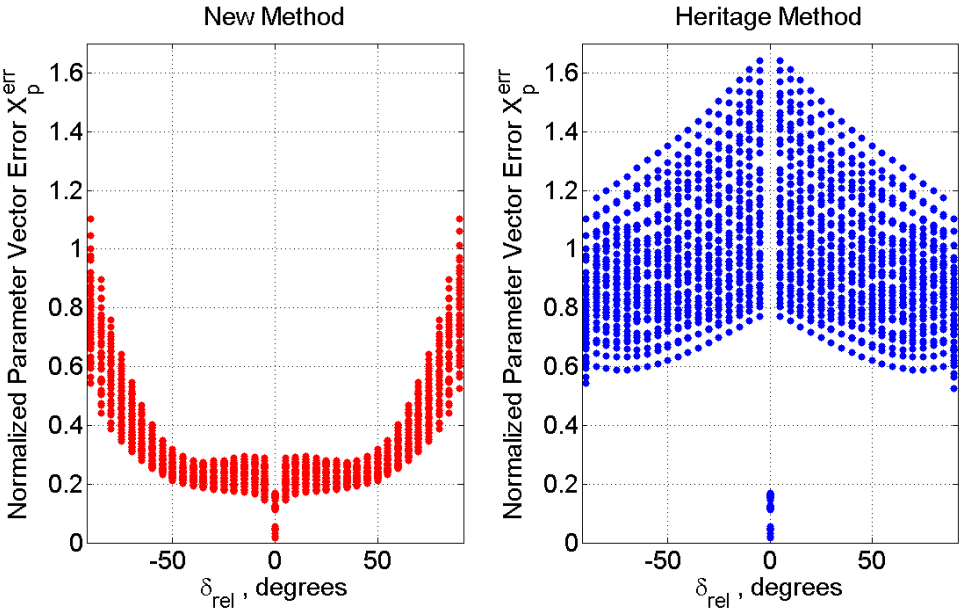

Figure 5. Improved Proximity of 3-Impulse Time-free IG to Optimal Through Reduction of Parameter Vector Error (X_p^{err}) vs. δ_{rel} over the Range Provided in Table 1.

Figures 6-7 demonstrate (for particular cases) that r_{a_1} tends to r_{max} and that r_{p_2} tends to r_{min} in the optimal solutions. Figure 7 also shows that $r_{p_3} = r_{p_f}$ is at or above the r_{min} boundary and therefore does not violate the constraint. At low δ_{rel} , $r_{p_3} = r_{p_2} = r_{min}$, but as the magnitude of δ_{rel} increases r_{p_3} grows larger and diverges from the r_{min} boundary, a fact indicative of possible cost savings through the addition of a fourth impulse, which will be discussed in section IV-D.

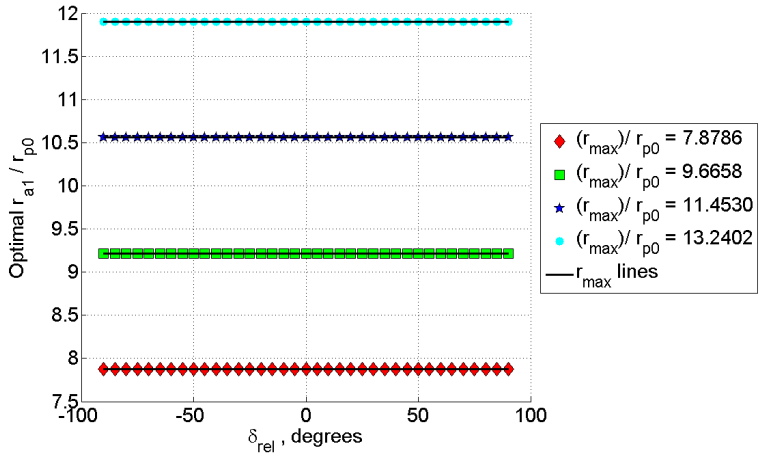

Figure 6. Optimal 3-Impulse Orbit 1 Apocenter Radii for $r_{min}/r_{p_0} = 0.8213$ and $v_\infty^+/v_{p_0} = 0.8106$ vs. δ_{rel} over the Range Provided in Table 1.

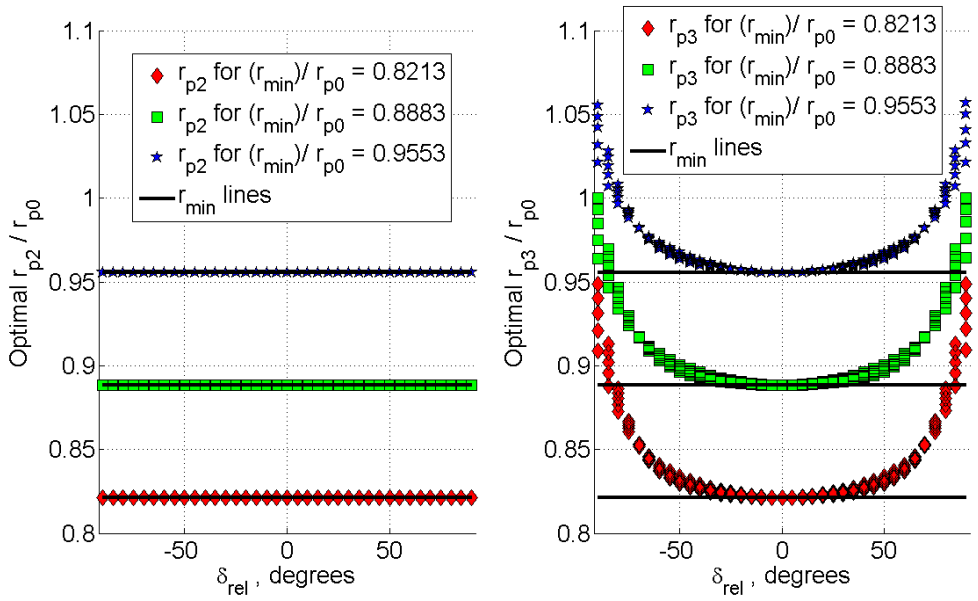

Figure 7. Optimal 3-Impulse Orbit 2/3 Pericenter Radii for $v_\infty^+/v_{p_0} = 0.8106$ and all r_{max}/r_{p_0} vs. δ_{rel} over the Range Provided in Table 1.

C. Time-Fixed 3-Impulse Escape Results

So that the following time-fixed results may be compared to those of the time-free 3-impulse escapes, the Table 1 scan was repeated with the TOF computed as a function of r_{max} and r_{min} such that,

$$TOF = 2\pi\sqrt{\left(\frac{r_{min} + r_{max}}{2}\right)^3 \frac{1}{\mu}} \tag{66}$$

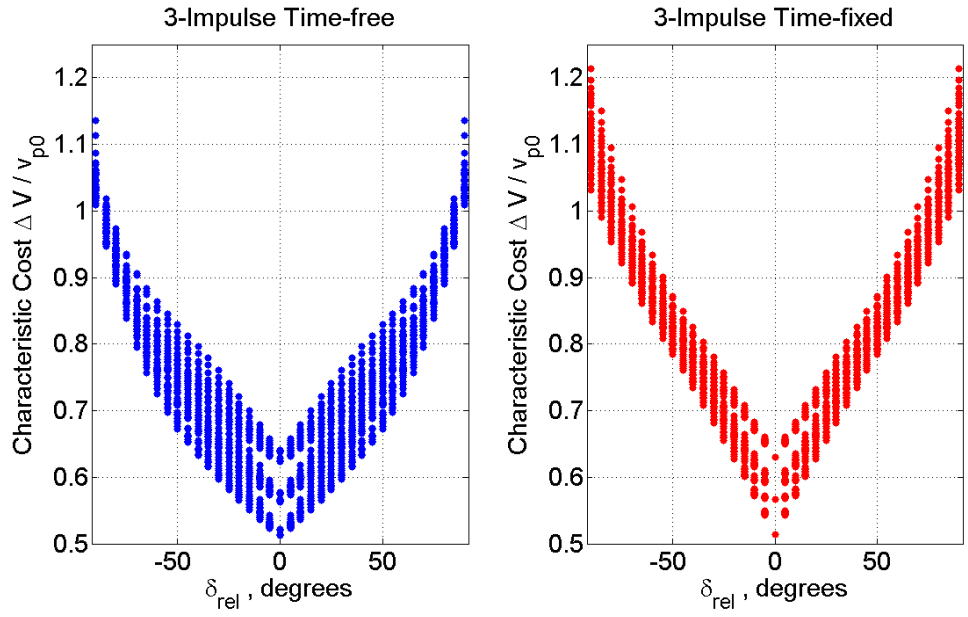

Figure 8. 3-Impulse Time-free and Time-fixed IG Characteristic Cost Comparison vs. δ_{rel} over the Range Provided in Table 1.

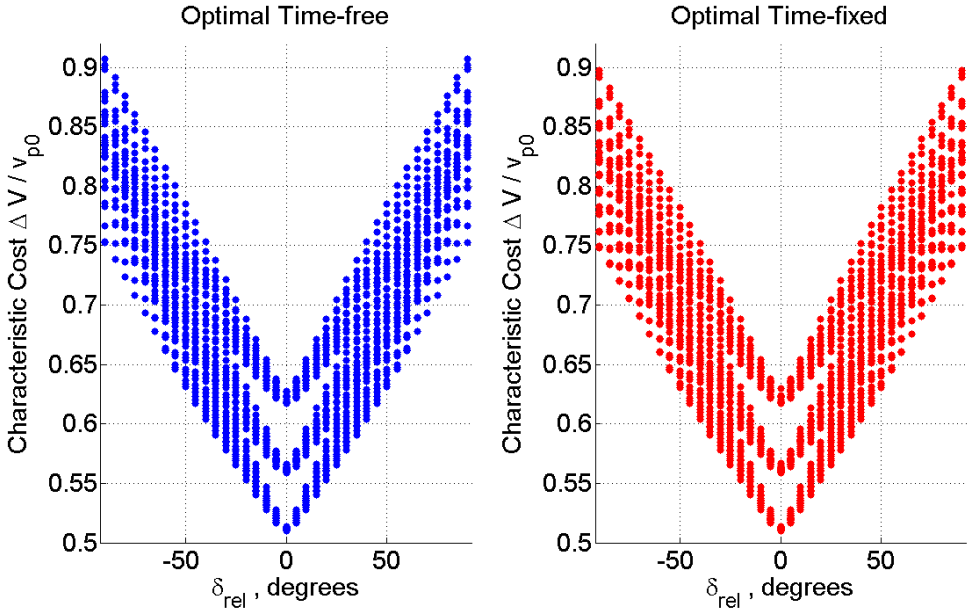

Figure 9. 3-Impulse Time-free and Time-fixed Optimal Characteristic Cost Comparison vs. δ_{rel} over the Range Provided in Table 1.

It is expected that the ΔV plots for the time-free and fixed IG methods should exhibit similar behavior, a fact confirmed in Figure 8. Furthermore, the optimal solutions associated with these initial guesses should be nearly identical, as demonstrated in Figure 9. The X_p^{err} for the two constructions, will however, be different since the parameter vectors are not the same and the IG constructions do differ. Figure 10 compares the two method's parameter vector errors, time-free X_p^{err} defined in Eq. (48) vs. time-fixed X_p^{err} as defined in Eq. (63). The larger error exhibited by the time-fixed method is due in part to maintaining $\hat{\mathbf{h}}_f = \hat{\mathbf{h}}_f^*$, resulting in a greater number of iterations to converge, discussed in section D. Figure 11 shows the total

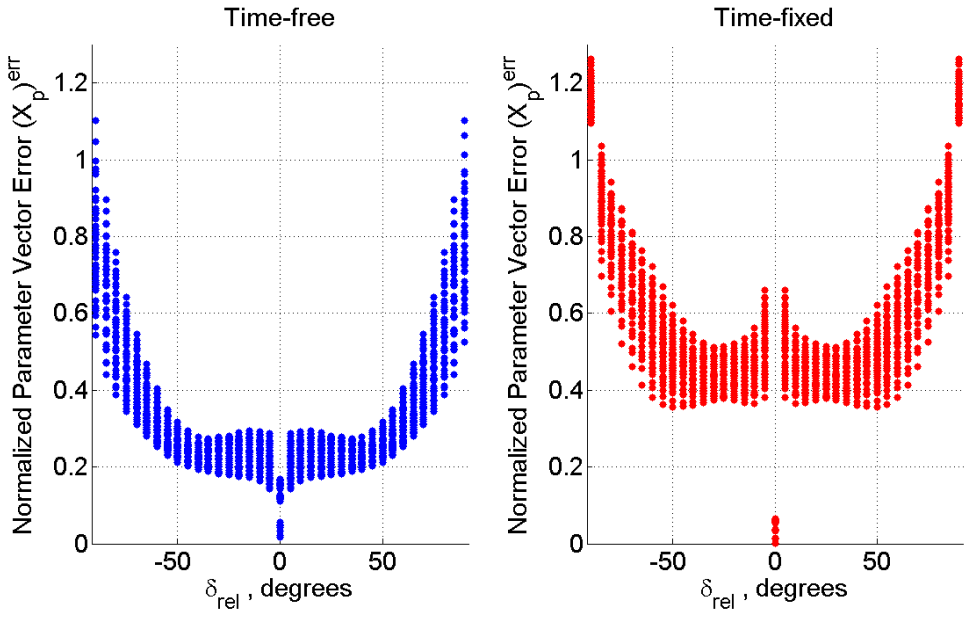

Figure 10. 3-Impulse Time-free and Time-fixed X_p^{err} Comparison vs. δ_{rel} over the Range Provided in Table 1.

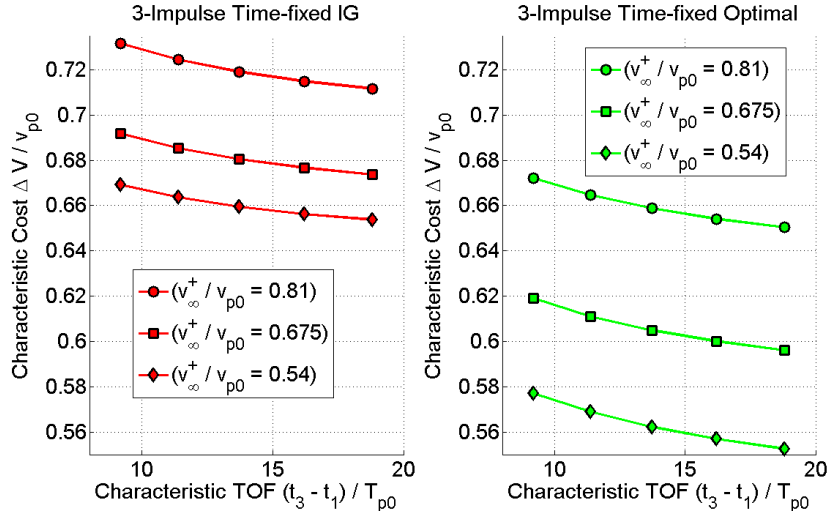

Figure 11. 3-Impulse Time-fixed IG and Optimal Characteristic Cost Comparison vs. TOF for $\delta_{rel} = 20°$, $r_{min}/r_{p_0} = 0.8213$ and all v_∞^+/v_{p_0} over the Range Provided in Table 1.

characteristic cost versus the characteristic TOF and v_∞^+/v_{p_0}, for a particular case of r_{min}/r_{p_0} and δ_{rel}. The cost decreases with increasing TOF and decreasing v_∞^+/v_{p_0}, as expected. For this particular case, the behavior of the optimal solutions are mimicked by the IG, but at a slightly higher ΔV.

D. How Many Impulses?

Although 1 and 3-impulse problems are constructed and can be converged to the optimum, the question of how many impulses to use for a given escape geometry remains. Jezewski and Rozendaal (among others) have considered this question from the perspective of primer vector theory, when the TOF is specified.[8] In the context of the time-free parameter optimization problem; however, very little has been published to answer this question. This section presents some simple qualitative switching criteria, which may be utilized to aid in the escape design. The first criteria, will be that of when to switch from 1 to 3-impulses. The

3-impulse escape yields much lower costs than the 1-impulse at high δ_{rel}, and so the most difficult region for determining switching is at low δ_{rel}. To illustrate this, another input parameter scan is utilized as defined in Table 2, with δ_{rel} now being the outermost loop and v_∞^+/v_{p_0} the innermost.

Input Parameter	Min. Value	Max. Value	Step Size
δ_{rel}	0°	10°	1°
r_{min}/r_{p_0}	0.3	1	0.4
r_{max}/r_{p_0}	5	10	2.5
v_∞^+/v_{p_0}	0.2344	1.6409	0.1172
r_{p_0}	6738.1 km	6738.1 km	0

Table 2. Input Parameter Scan Used to Generate 1/3 Impulse Switching Criteria Plots

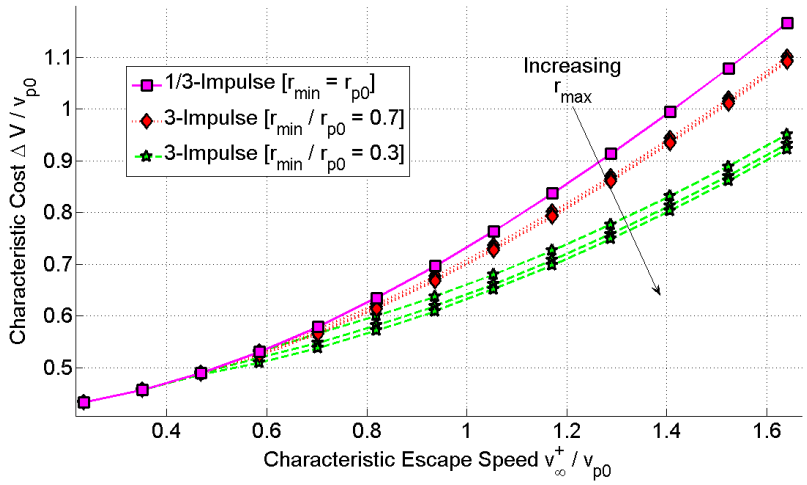

Figure 12. 1/3 Impulse Switching Criteria: Characteristic Cost vs. Characteristic Escape Speed at $\delta_{rel} = 0°$ over the Range Provided in Table 2.

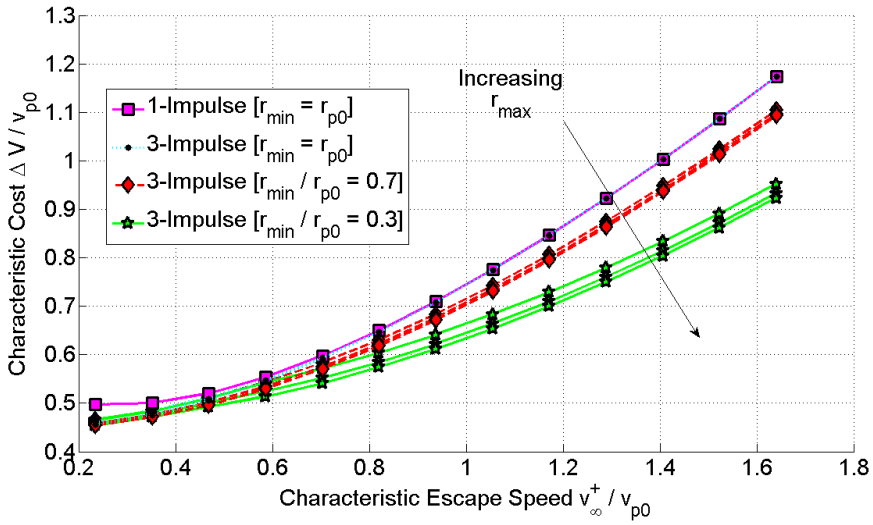

Figure 13. 1/3 Impulse Switching Criteria: Characteristic Cost vs. Characteristic Escape Speed at $\delta_{rel} = 5°$ over the Range Provided in Table 2.

As stated previously, and cited for example in[4] and,[1] when the orbit planes are coincident and $r_{min} = r_{p_0}$, the 1-impulse escape will yield the same cost but with a much shorter TOF. When $r_{min} \neq r_{p_0}$, the criteria for switching is a function of v_∞^+/v_{p_0} and the pericenter/apocenter limits r_{min} and r_{max}, a fact noted in.[4] Figures 12-14 compare the optimum characteristic costs of the 1 and 3-impulse escapes for the range of inputs given in Table 2, and $\delta_{rel} = 0°$, 5°, and 10°.

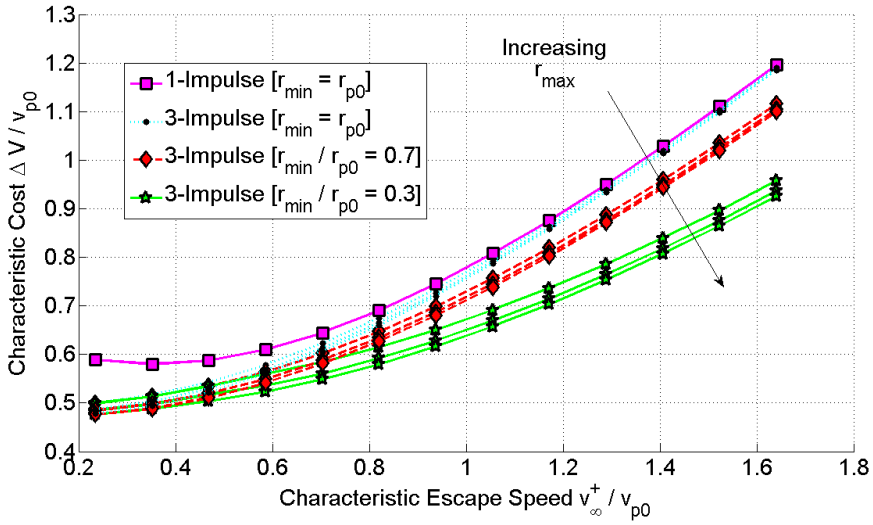

Figure 14. 1/3 Impulse Switching Criteria: Characteristic Cost vs. Characteristic Escape Speed at $\delta_{rel} = 10°$ over the Range Provided in Table 2.

Based on these results, the 3-impulse escape will be of lower cost if $v_\infty^+/v_{p_0} \geq 0.8$ and $r_{min} < r_{p_0}$. Recall, however, that this may not hold in the presence of gravitational perturbations or in constructing a complete trajectory. In fact, it has been shown in,[2] that a 1-impulse escape can be cheaper than a 3-impulse for δ_{rel} as high as 12°, when the effect of the Earth is included.

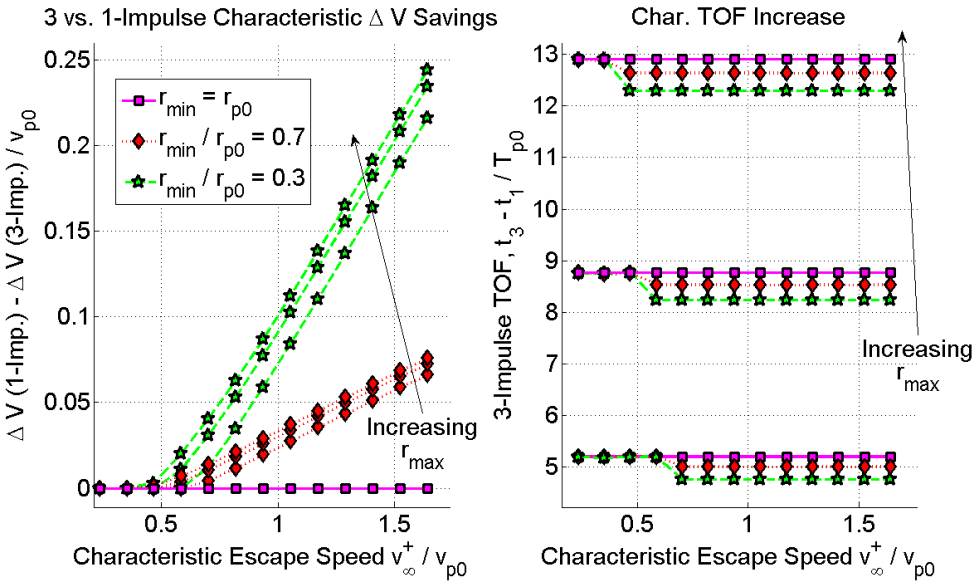

Figure 15. 1/3 Impulse Switching Criteria at $\delta_{rel} = 0°$ over the Range Provided in Table 2: a) Characteristic Cost Savings and b) Characteristic TOF Increase ($(t_3 - t_1)/T_{p_0}$).

Another consideration to be made, is that at low δ_{rel} the savings in ΔV may be small compared with the increased TOF when switching from a 1 to a 3-impulse escape. Figures 15-17 present data which would

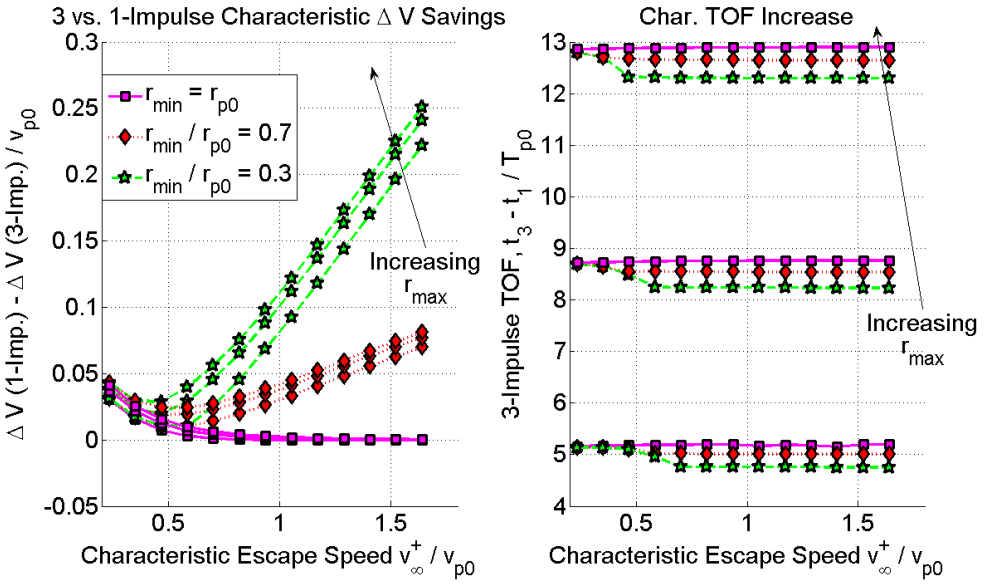

Figure 16. 1/3 Impulse Switching Criteria at $\delta_{rel} = 5°$ over the Range Provided in Table 2: a) Characteristic Cost Savings and b) Characteristic TOF Increase ($(t_3 - t_1)/T_{p_0}$).

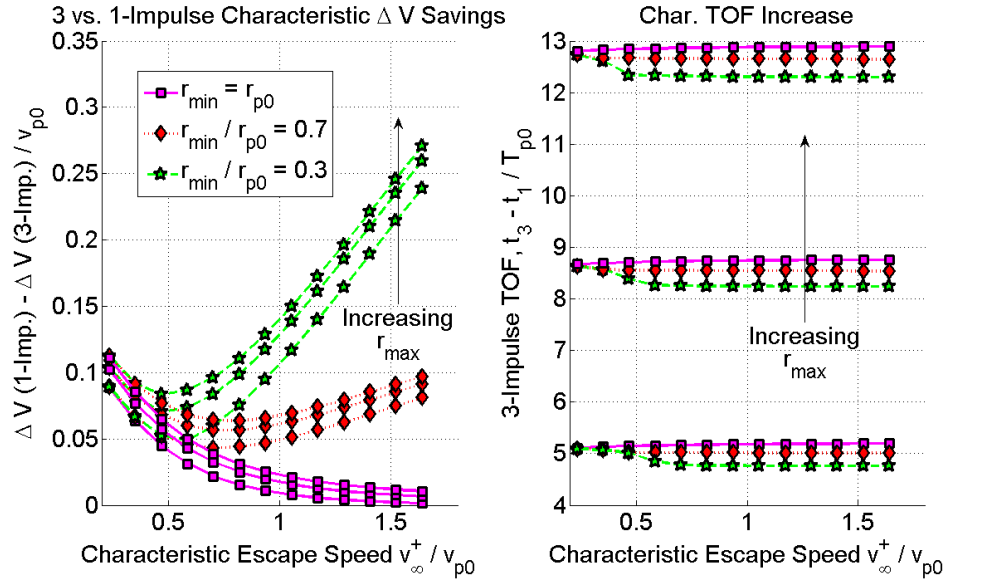

Figure 17. 1/3 Impulse Switching Criteria at $\delta_{rel} = 10°$ over the Range Provided in Table 2: a) Characteristic Cost Savings and b) Characteristic TOF Increase ($(t_3 - t_1)/T_{p_0}$).

be useful in making this trade as applied to a real mission, for the same δ_{rel} values as before. The plots therefore indicate the non-dimensional cost savings versus the added non-dimensional TOF when using a 3-impulse escape over a 1-impulse escape.[¶] For example, in Figure 16 at $v_\infty^+/v_{p_0} = 1.0$ and $r_{min}/r_{p_0} = 0.7$ the characteristic cost savings are just above 0.05 but the characteristic TOF increase can be anywhere from 5 to 13, depending on the choice of r_{max}.

As δ_{rel} gets exceedingly large a 4th impulse may provide a lower cost escape than the 3-impulse. For circular parking orbits and $r_{min} \leq r_{p_0}$, Edelbaum[5] provides a simple measure for whether a 3 or 4-impulse escape should be used based on the minimum plane change angle θ, given in Eq. (21), and the true

[¶]The 1-impulse TOF is considered to be zero and therefore the increased TOF is simply the 3-impulse $TOF = t_3 - t_1$ made non-dimensional through division by the parking orbit period T_{p_0}

anomaly associated with $\mathbf{v}_\infty^+$ on the departure hyperbola ν_∞^+, given in Eq. (9). This criteria is derived using asymptotic expansions of the total cost when the TOF is known. As alluded to before, those cases where a 4th impulse should be added, correspond to the same cases where r_{p_3} is diverging from r_{min} in Figure 7.

$$\text{If,} \qquad \theta \; < \; \pi - \nu_\infty^+ \qquad \text{Then a 3-impulse escape is indeed optimal.}$$

Otherwise adding a 4th impulse may reduce the cost. Based on this criteria, the optimal 3-impulse characteristic costs from Figure 4 are repeated in Figure 18, but those escapes where the 3-impulse are indeed optimum (left plot) are differentiated from those where a 4th impulse should be added (right plot). It should be noted that these savings must still be verified and quantified.

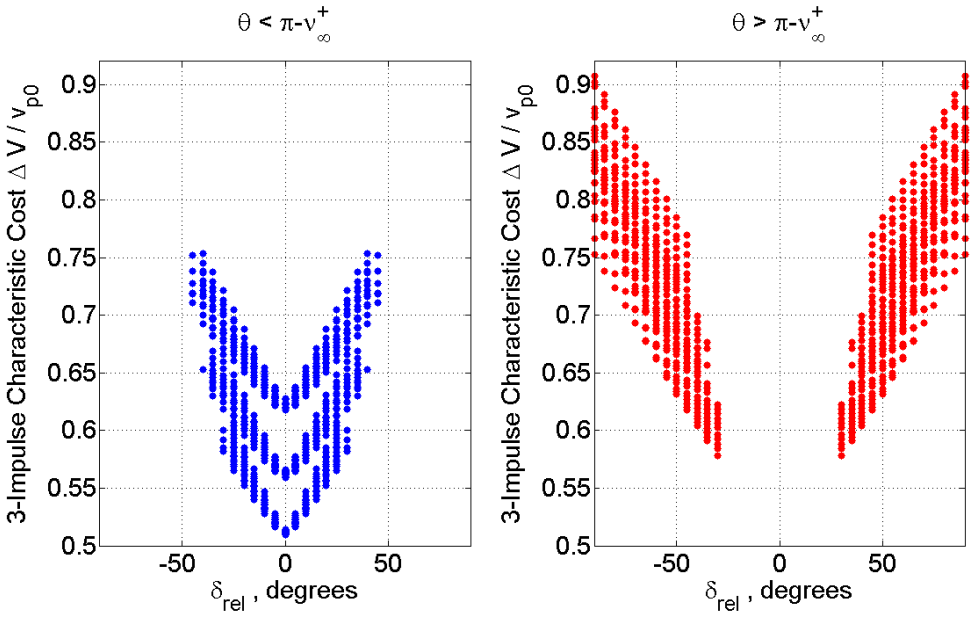

Figure 18. 3/4 Impulse Switching Criteria: Optimal 3-Impulse Characteristic Cost vs. δ_{rel} over the Range Provided in Table 1.

Table 3 compares all of the impulsive escape methods and their convergence to the optimal solutions over the input parameter ranges given in Table 1. These comparisons are as valid as possible, in that the tuning, scaling, and method for converging each optimization problem was kept as similar as possible. From

Impulsive Escape Type	**Avg. Opt. $\Delta V/v_{p_0}$**	**Avg. Opt. TOF/T_{p_0}**	**Avg. X_p^{err}**	**Avg. Num. of Iterations**
Single-Impulse	1.2075	n/a	0.2450	13
3-Impulse Time-free with $\mathbf{\Delta v}_3$ in $\mathbf{X_p}$	0.6914	13.6104	0.3364	3393
3-Impulse Time-free without $\mathbf{\Delta v}_3$ in $\mathbf{X_p}$	0.6914	13.6104	0.3237	3180
3-Impulse Time-fixed	0.6897	13.8354	0.5720	10900

Table 3. Summary of Averaged Optimal Impulsive Escapes and Convergence for all Methods over the Range Provided in Table 1.

Table 3, it is noted that over the entire range of scanned parameters the 3-impulse escape has a much lower average characteristic cost $\Delta V/v_{p_0}$, but that this comes at the expense of added flight time (TOF), and a two orders of magnitude increase in the average number of iterations required to converge upon the optimal. When $\mathbf{\Delta v}_3$ is explicitly removed from the 3-impulse time-free $\mathbf{X_p}$ the number of iterations required decreases some, but not substantially. The 3-impulse time-fixed construction exhibits the greatest average X_p^{err} and therefore requires many more iterations to converge to the optimal. This is due in part to a relatively poor

selection of $\hat{\mathbf{h}}_f$ and the intermediate Orbits' line of apses in the IG, which were necessary to satisfy the TOF explicitly. The optimal solutions may still be converged upon, however this construction may best be utilized to provide quick initial cost estimates as a function of TOF.

V. Conclusions

Methods for determining optimal impulsive transfers from a circular parking orbit about an arbitrary celestial body to some excess velocity vector $\mathbf{v}_\infty^+$ have been presented. Non-dimensional parameters have been used throughout this work, so that the results and methods may be applied to escapes from any celestial body and to all relative declination, right ascension, and v_∞^+ magnitude targets. Constrained parameter optimization problems are constructed and solved, but generally require a quality initial guess (IG), resulting in the introduction of the non-dimensional parameter vector error (X_p^{err}) in order to assess IG proximity to the optimal. The 3-impulse IG method has been dramatically improved from that of,[2] and now more closely reflects the behavior of the optimal resulting in better overall convergence.

The 3-impulse time-fixed IG and optimization method developed in this work will allow for quick cost assessments for a variety of escape geometries as a function of the time-of-flight (TOF). In addition, the qualitative criteria developed will enable the determination of whether a 3-impulse escape should be used over a 1-impulse escape, which generally involves trading ΔV reduction with TOF increase. The feasible/optimal impulsive escapes developed may be used as quality initial guesses for larger problems involving: continuous transfers between celestial bodies in an N-body gravitational field, conversion to optimal finite-burn escapes, and combinations of the two.

The methods and results presented in this paper are currently being used to investigate further improvements to the IG constructions as e_0 increases from zero and α_{rel} becomes increasingly important. The switching criteria between 1 and 3-impulse escapes will also have to be updated when considering parking orbits with $e_0 \neq 0$. Following the methodology of the 1 and 3-impulse time-free escapes, a 4-impulse IG and optimization construction is being investigated in order to validate the claims made in[5] that additional savings can be obtained (from that of the 3-impulse) for certain escape geometries. Furthermore, the switching criteria from 3-impulses to 4 may also involve increased TOF, and any ΔV savings may vary dramatically for $e_0 \neq 0$, all of which must be investigated.

Acknowledgment

The authors wish to thank Sonia Hernandez for crucial assistance in the early development of these methods and for her valuable comments and editing work. Much thanks to Mr. Gerald Condon of the NASA Johnson Space Center for his role as Technical Supervisor of NASA's grant NNX08AN02G, which supports this research. Finally, D.R. Jones would like to thank his future wife Ashlee Kamins for her constant support and encouragement.

References

[1]Gerbracht, R.J. and Penzo, P.A., "Optimum Three-Impulse Transfer Between an Elliptic Orbit and a Non-Coplanar Escape Asymtote," *AAS/AIAA Astrodynamics Specialist Conference*, American Astronomical Society Paper 68-084, Jackson, WY, Sept. 1968.

[2]Ocampo, C. and Saudemont, R., "Initial Trajectory Model for a Multi-Maneuver Moon-to-Earth Abort Sequence," *Journal of Guidance, Control, and Dynamics*, Vol. 33, No. 4, July-August 2010, pp. 1184-1194.

[3]Lawden, D., *Optimal Trajectories for Space Navigation*, Butterworths, London, 1963.

[4]Gobetz, F.W. and Doll, J.R., "A Survey of Impulsive Trajectories, Final Report," United Aircraft Research Laboratories, Tech. Rept. G-910557-11, 1968.

[5]Edelbaum, T.N., "Optimal Nonplanar Escape from Circular Orbits," *AIAA Journal*, Vol. 9, No. 12, 1971, pp. 2432-2436.

[6]Condon, G., et al., "CEV Trajectory Design Considerations for Lunar Missions," *AAS/AIAA Guidance, Navigation, and Control Conference*, February 2007, Breckenridge, Colorado, AAS 07-075.

[7]Bate, R. R., Mueller, D. D., and White, J. E., *Fundamentals of Astrodynamics*, Dover, New York, 1971.

[8]Jezewski, D. and Rozendaal, H., "An Efficient Method for Calculating Optimal Free-Space N-Impulse Trajectories," *AIAA Journal*, December 1967, pp. 2160-2165.